

Measurement of small angle antiproton-proton elastic scattering at $\sqrt{s} = 546$ and 1800 GeV

- F. Abe,¹² M. Albrow,⁶ D. Amidei,¹⁵ C. Anway-Wiese,³ G. Apollinari,²³ M. Atac,⁶
 P. Auchincloss,²² P. Azzi,¹⁷ N. Bacchetta,¹⁶ A. R. Baden,⁸ W. Badgett,¹⁵
 M. W. Bailey,²¹ A. Bamberger,^{6,*} P. de Barbaro,²² A. Barbaro-Galtieri,¹³
 V. E. Barnes,²¹ B. A. Barnett,¹¹ G. Bauer,¹⁴ T. Baumann,⁸ F. Bedeschi,²⁰
 S. Behrends,² S. Belforte,²⁰ G. Bellettini,²⁰ J. Bellinger,²⁸ D. Benjamin,²⁷
 J. Benlloch,¹⁴ J. Bensinger,² A. Beretvas,⁶ J.P. Berge,⁶ S. Bertolucci,⁷ K. Biery,¹⁰
 S. Bhadra,⁹ M. Binkley,⁶ D. Bisello,¹⁷ R. Blair,¹ C. Blocker,² A. Bodek,²²
 V. Bolognesi,²⁰ A. W. Booth,⁶ C. Boswell,¹¹ G. Brandenburg,⁸ D. Brown,⁸
 E. Buckley-Geer,⁶ H. S. Budd,²² G. Busetto,¹⁷ A. Byon-Wagner,⁶ K. L. Byrum,¹
 C. Campagnari,⁶ M. Campbell,¹⁵ A. Caner,⁶ R. Carey,⁸ W. Carithers,¹³
 D. Carlsmith,²⁸ J. T. Carroll,⁶ R. Cashmore,^{6,*} A. Castro,¹⁷ Y. Cen,¹⁸ F. Cervelli,²⁰
 K. Chadwick,⁶ J. Chapman,¹⁵ T. J. Chapin,²³ G. Chiarelli,⁷ W. Chinowsky,¹³
 S. Cihangir,⁶ A. G. Clark,⁶ M. Cobl,²⁰ D. Connor,¹⁸ M. Contreras,⁴
 J. Cooper,⁶ M. Cordelli,⁷ D. Crane,⁶ J. D. Cunningham,² C. Day,⁶ F. DeJongh,⁶
 S. Dell'Agnello,²⁰ M. Dell'Orso,²⁰ L. Demortier,²³ B. Denby,⁶ P. F. Derwent,¹⁵
 T. Devlin,²⁴ M. Dickson,²² R. B. Drucker,¹³ A. Dunn,¹⁵ K. Einsweiler,¹³ J. E. Elias,⁶
 R. Ely,¹³ S. Eno,⁴ S. Errede,⁹ A. Etchegoyen,^{6,*} B. Farhat,¹⁴ M. Frautschi,¹⁶
 G. J. Feldman,⁸ B. Flaughner,⁶ G. W. Foster,⁶ M. Franklin,⁸ J. Freeman,⁶
 T. Fuess,⁶ Y. Fukui,¹² A. F. Garfinkel,²¹ A. Gauthier,⁹ S. Geer,⁶ D. W. Gerdes,¹⁵
 P. Giannetti,²⁰ N. Giokaris,²³ P. Giromini,⁷ L. Gladney,¹⁸ M. Gold,¹⁶ J. Gonzalez,¹⁸
 K. Goulios,²³ H. Grassmann,¹⁷ G. M. Grieco,²⁰ R. Grindley,¹⁰ C. Grosso-Pilcher,⁴
 C. Haber,¹³ S. R. Hahn,⁶ R. Handler,²⁸ K. Hara,²⁶ B. Harral,¹⁸
 R. M. Harris,⁶ S. A. Hauger,⁵ J. Hauser,³ C. Hawk,²⁴ T. Hessing,²⁵ R. Hollebeek,¹⁸
 L. Holloway,⁹ A. Holscher,¹⁰ S. Hong,¹⁵ G. Houk,¹⁸ P. Hu,¹⁹ B. Hubbard,¹³
 B. T. Huffman,¹⁹ R. Hughes,²² P. Hurst,⁸ J. Huth,⁶ J. Hysten,⁶ M. Incagli,²⁰
 T. Ino,²⁶ H. Iso,²⁶ C. P. Jessop,⁸ R. P. Johnson,⁶ U. Joshi,⁶ R. W. Kadel,¹³
 T. Kamon,²⁵ S. Kanda,²⁶ D. A. Kardelis,⁹ I. Karliner,⁹ E. Kearns,⁸ L. Keeble,²⁵
 R. Kephart,⁶ P. Kesten,² R. M. Keup,⁹ H. Keutelian,⁶ D. Kim,⁶ S. B. Kim,¹⁵
 S. H. Kim,²⁶ Y. K. Kim,¹³ L. Kirsch,² K. Kondo,²⁶ J. Konigsberg,⁸ K. Kordas,¹⁰
 E. Kovacs,⁶ M. Krasberg,¹⁵ S. E. Kuhlmann,¹ E. Kuns,²⁴ A. T. Laasanen,²¹
 S. Lammel,³ J. I. Lamoureux,²⁸ S. Leone,²⁰ J. D. Lewis,⁶ W. Li,¹ P. Limon,⁶
 M. Lindgren,³ T. M. Liss,⁹ N. Lockyer,¹⁸ M. Loreti,¹⁷ E. H. Low,¹⁸ D. Lucchesi,²⁰
 C. B. Luchini,⁹ P. Lukens,⁶ P. Maas,²⁸ K. Maeshima,⁶ M. Mangano,²⁰ J. P. Marriner,⁶
 M. Mariotti,²⁰ R. Markeloff,²⁸ L. A. Markosky,²⁸ J. A. J. Matthews,¹⁶ R. Mattingly,²
 C. McClure,⁶ P. McIntyre,²⁵ A. Menzione,²⁰ E. Meschi,²⁰ T. Meyer,²⁵ S. Mikamo,¹²
 M. Miller,⁴ T. Mimashi,²⁶ S. Miscetti,⁷ M. Mishina,¹² S. Miyashita,²⁶ Y. Morita,²⁶
 S. Moulding,²³ J. Mueller,²⁴ A. Mukherjee,⁶ T. Muller,³ L. F. Nakae,² I. Nakano,²⁶
 C. Nelson,⁶ D. Neuberger,³ C. Newman-Holmes,⁶ J. S. T. Ng,⁸ M. Ninomiya,²⁶
 L. Nodulman,¹ S. Ogawa,²⁶ R. Paoletti,²⁰ V. Papadimitriou,⁶ A. Para,⁶ E. Pare,⁸
 S. Park,⁶ J. Patrick,⁶ G. Pauletta,²⁰ L. Pescara,¹⁷ T. J. Phillips,⁵ A. G. Piacentino,²⁰ R. Plunkett,⁶
 L. Pondrom,²⁸ J. Proudfoot,¹ F. Ptohos,⁸ G. Punzi,²⁰ D. Quarrie,⁶
 K. Ragan,¹⁰ G. Redlinger,⁴ J. Rhoades,²⁸ M. Roach,²⁷ F. Rimondi,^{6,*} L. Ristori,²⁰
 W. J. Robertson,⁵ T. Rodrigo,⁶ T. Rohaly,¹⁸ A. Roodman,⁴ W. K. Sakumoto,²²
 A. Sansoni,⁷ R. D. Sard,⁹ A. Savoy-Navarro,⁶ V. Scarpine,⁹ P. Schlabach,⁸
 E. E. Schmidt,⁶ O. Schneider,¹³ M. H. Schub,²¹ R. Schwitters,⁸ G. Sciacca,²⁰
 A. Scribano,²⁰ S. Segler,⁶ S. Seidel,¹⁶ Y. Seiya,²⁶ G. Sganos,¹⁰ N. M. Shaw,²¹
 M. Sheaff,²⁸ M. Shochet,⁴ J. Siegrist,¹³ A. Sill,²² P. Sinervo,¹⁰ J. Skarha,¹¹
 K. Sliwa,²⁷ D. A. Smith,²⁰ F. D. Snider,¹¹ L. Song,⁶ T. Song,¹⁵ M. Spahn,¹³
 P. Sphicas,¹⁴ A. Spies,¹¹ R. St. Denis,⁸ L. Stanco,¹⁷ A. Stefanini,²⁰ G. Sullivan,⁴
 K. Sumorok,¹⁴ R. L. Swartz, Jr.,⁹ M. Takano,²⁶ K. Takikawa,²⁶ S. Tarem,²
 F. Tartarelli,²⁰ S. Tether,¹⁴ D. Theriot,⁶ M. Timko,²⁷ P. Tipton,²² S. Tkaczyk,⁶
 A. Tollestrup,⁶ J. Tonnison,²¹ W. Trischuk,⁸ Y. Tsay,⁴ J. Tseng,¹¹ N. Turini,²⁰
 F. Ukegawa,²⁶ D. Underwood,¹ S. Vejck III,¹⁵ R. Vidal,⁶ R. G. Wagner,¹
 R. L. Wagner,⁶ N. Wainer,⁶ R. C. Walker,²² J. Walsh,¹⁸ A. Warburton,¹⁰

*Visitor.

G. Watts,²² T. Watts,²⁴ R. Webb,²⁵ C. Wendt,²⁸ H. Wenzel,²⁰ W. C. Wester III,¹³
 T. Westhusing,⁹ S. N. White,²³ A. B. Wicklund,¹ E. Wicklund,⁶ H. H. Williams,¹⁸
 B. L. Winer,²² J. Wolinski,²⁵ D. Y. Wu,¹⁵ X. Wu,²⁰ J. Wyss,¹⁷ A. Yagil,⁶
 K. Yasuoka,²⁶ Y. Ye,¹⁰ G. P. Yeh,⁶ J. Yoh,⁶ M. Yokoyama,²⁶ J. C. Yun,⁶
 A. Zanetti,²⁰ F. Zetti,²⁰ S. Zhang,¹⁵ W. Zhang,¹⁸ and S. Zucchelli^{6,*}

(CDF Collaboration)

¹Argonne National Laboratory, Argonne, Illinois 60439

²Brandeis University, Waltham, Massachusetts 02254

³University of California at Los Angeles, Los Angeles, California 90024

⁴University of Chicago, Chicago, Illinois 60637

⁵Duke University Durham, North Carolina 27706

⁶Fermi National Accelerator Laboratory, Batavia, Illinois 60510

⁷Laboratori Nazionali di Frascati, Istituto Nazionale di Fisica Nucleare, Frascati, Italy

⁸Harvard University, Cambridge, Massachusetts 02138

⁹University of Illinois, Urbana, Illinois 61801

¹⁰Institute of Particle Physics, McGill University, Montreal, and University of Toronto, Toronto, Canada

¹¹The Johns Hopkins University, Baltimore, Maryland 21218

¹²National Laboratory for High Energy Physics (KEK), Japan

¹³Lawrence Berkeley Laboratory, Berkeley, California 94720

¹⁴Massachusetts Institute of Technology, Cambridge, Massachusetts 02139

¹⁵University of Michigan, Ann Arbor, Michigan 48109

¹⁶University of New Mexico, Albuquerque, New Mexico 87131

¹⁷Universita di Padova, Istituto Nazionale di Fisica Nucleare, Sezione di Padova, I-35131 Padova, Italy

¹⁸University of Pennsylvania, Philadelphia, Pennsylvania 19104

¹⁹University of Pittsburgh, Pittsburgh, Pennsylvania 15260

²⁰Istituto Nazionale di Fisica Nucleare, University and Scuola Normale Superiore of Pisa, I-56100 Pisa, Italy

²¹Purdue University, West Lafayette, Indiana 47907

²²University of Rochester, Rochester, New York 14627

²³Rockefeller University, New York, New York 10021

²⁴Rutgers University, Piscataway, New Jersey 08854

²⁵Texas A&M University, College Station, Texas 77843

²⁶University of Tsukuba, Tsukuba, Ibaraki 305, Japan

²⁷Tufts University, Medford, Massachusetts 02115

²⁸University of Wisconsin, Madison, Wisconsin 53706

(Received 5 August 1993)

Antiproton-proton elastic scattering was measured at c.m.s. energies $\sqrt{s} = 546$ and 1800 GeV in the range of four-momentum transfer squared $0.025 < -t < 0.29$ GeV². The data are well described by the exponential form e^{bt} with a slope $b = 15.28 \pm 0.58$ (16.98 ± 0.25) GeV⁻² at $\sqrt{s} = 546$ (1800) GeV. The elastic scattering cross sections are, respectively, $\sigma_{el} = 12.87 \pm 0.30$ and 19.70 ± 0.85 mb.

PACS number(s): 13.85.Dz

I. INTRODUCTION

This paper, describing the measurement of the $\bar{p}p$ elastic scattering differential cross section at the Fermilab Tevatron Collider, is the first of three related papers [1,2] leading to the measurement of the elastic, diffractive, and total cross sections for $\bar{p}p$ collisions using the luminosity-independent method. During the 1988–1989 physics run of the Fermilab Tevatron Collider, the $\bar{p}p$ elastic scattering differential cross section was measured in the four-momentum transfer-squared range $0.025 < -t < 0.29$ GeV² at c.m. system (c.m.s.) energies $\sqrt{s} = 546$ and 1800 GeV. The data were taken in short dedicated runs, in which the Tevatron lattice was adjusted to provide low- t detection over a wide t range at each energy. After an initial run at $\sqrt{s} = 1800$, one run at $\sqrt{s} = 546$ was followed immediately by a second run

at $\sqrt{s} = 1800$. At these energies, the average scattering angle is a fraction of a mrad. Therefore, this measurement required that detectors were brought as close as 4 mm to the beam axis with an accuracy of $\simeq 10$ μ m and at distances of $\simeq 30$ m from the interaction region; as the detectors lay in between several Tevatron magnets, a precision measurement required the determination of the transport matrices of this sector of the machine to one part in a thousand.

II. EXPERIMENTAL METHOD

A top view of the experimental layout is shown in Fig. 1. Elastically scattered particles were observed by a magnetic spectrometer composed of two arms in the (horizontal) x - z plane of the machine: arm 1 detected elastic

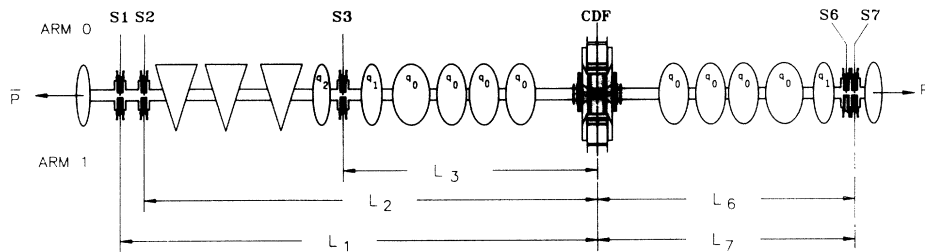


FIG. 1. Top view of the elastic scattering setup. Values of the focal lengths L_i are listed in Table I.

events in which the $\bar{p}(p)$ was scattered towards the inside (outside) of the beam orbit; with respect to the beam z axis, symmetrically scattered elastic events were detected by arm 0. We call *west* the outgoing \bar{p} side (positive z axis) and *east* the outgoing p side; y is the vertical axis pointing up. In each arm, the \bar{p} trajectory was measured at three different z positions along the beam line by detectors $S3$, $S2$, and $S1$, while the p path was determined by the $S6$ and $S7$ detectors. In elastic events, the proton and antiproton are collinear and one detector on each side would be enough to make a measurement. The redundancy in our detectors guarantees full efficiency and reduces systematic errors. All detectors were placed inside special sections of the beam pipe with variable aperture. Once stable beam conditions were reached, the detectors were displaced horizontally towards the circulating beam. The beam was scraped until the detectors could reach the desired positions. Detector displacements were monitored with an accuracy better than $10 \mu\text{m}$. From survey measurements, the detector distances from the machine magnetic axis were known to $\pm 0.1 \text{ mm}$; distances from the interaction point were determined to $\pm 1 \text{ cm}$ and distances between two detectors in different arms at the same z location were surveyed to within $70 \mu\text{m}$.

Elastically scattered recoils traveled through the quadrupole magnets q_0 , q_1 , and q_2 . The magnets q_1 defocused (D) and q_2 focused (F) in the horizontal plane. The string of four FDDF quadrupoles q_0 on each side of the interaction region provided high luminosity by squeezing the betatron function at the interaction region to a value $\beta \simeq 0.5 \text{ m}$ (low β). In the $\sqrt{s} = 546$ run, the magnets q_0 were almost at full power. In the two $\sqrt{s} = 1800$ runs, the q_0 's were powered off and β was about 80 m at the interaction region (high β). Using the standard formalism of transfer matrices, the elastic recoil coordinates at a given z_i position are

$$\begin{aligned} x_i &= \epsilon_i^h x_0 + L_i^h \theta_x, \\ y_i &= \epsilon_i^v y_0 + L_i^v \theta_y, \end{aligned} \quad (1)$$

where (x_0, y_0) are the coordinates at $z = 0$ and θ is the scattering angle. Values of the transfer matrix elements (ϵ_i, L_i) at the z position of each detector are listed in Table I. Each spectrometer detector (Fig. 2) comprised a drift chamber and a silicon detector sandwiched by two scintillation counters and had an active area $\Delta x \Delta y = 3.5 \times 3.0 \text{ cm}^2$. The drift chambers [3] had four wires measuring the x coordinate of a track at four different z positions. The sense wires induced signals on a delay line, which were used to measure the y coordinate by the time difference at the two ends. The drift measurement provided single-hit accuracy of $110 \mu\text{m}$ and double-hit resolution of 3 mm , while the single-hit accuracy of the delay line was $480 \mu\text{m}$ and the double-hit resolution about 2 cm .

The 0.9-mm -thick silicon detector [4] had double sided segmented read-out. The anode (ohmic side) consisted of 64 Al strips $50 \mu\text{m}$ wide, spaced by $500 \mu\text{m}$. By not completely depleting the diode, the x position was measured by the charge division method. The cathode (barrier side) measured the y position with 30 gold pads $900 \mu\text{m}$ wide, spaced by $100 \mu\text{m}$. The x resolution of the silicon detector turned out to be slightly worse than the pitch itself, but the double-hit resolution (1.0 mm in x and y) was very useful. The correlation between the charge collected by the cathode strips and by the anode pads allowed unambiguous reconstruction of multihit events. The accuracy (a few microns) to which the electrode positions were known allowed a good calibration of the drift velocity and of the delay line propagation time for every chamber. While taking data we lost some silicon channels; apart from that, both chamber and silicon detectors were 100% efficient (see Appendix A). The redundancy of active devices in each detector guaranteed full efficiency. The trigger for elastic events required the coincidence of all ten scintillation counters in each arm. To ensure full efficiency, test data were taken before each run and the voltage of each counter was adjusted so that its full pulse height spectrum was above threshold (see also Appendix A).

TABLE I. Transport matrix elements.

z (cm)		$\sqrt{s}=546$				$\sqrt{s}=1800$			
		ϵ^h	L^h (cm)	ϵ^v	L^v (cm)	ϵ^h	L^h (cm)	ϵ^v	L^v (cm)
5849.0	S1	-0.524	1719.8	-2.861	982.0	1.204	5698.8	0.077	4029.7
5544.2	S2	-0.404	1918.3	-2.542	981.8	1.224	5533.8	0.150	3827.5
3122.0	S3	0.478	3019.7	-0.126	1115.4	1.197	3667.7	0.810	2597.0
-3089.3	S6	-0.099	-1131.3	0.484	-2989.0	0.829	-2615.4	1.178	-3581.3
-3182.4	S7	-0.177	-1086.0	0.467	-3076.4	0.777	-2562.9	1.233	-3827.1

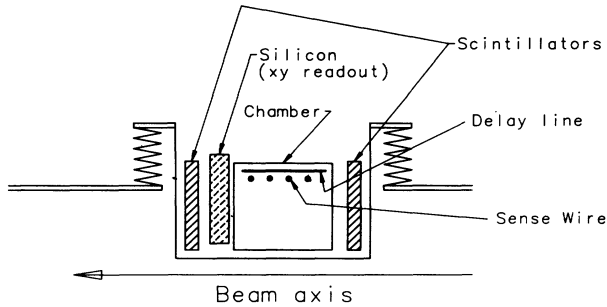


FIG. 2. Sketch of a detector assembly (top view); the detector section symmetric with respect to the beam axis is not shown.

III. DATA REDUCTION

A. Event reconstruction

We first reconstructed (x, y) points in every detector. In the silicon, we looked at the strips and reconstructed all charge clusters. For every cluster the x position (x_{sil}) was derived by charge weighting; by correlating the charges of the x clusters and of the y pads, space points were reconstructed. In the drift chamber, the x position was derived by requiring at least two out of four wires to have the same drift time (x_{drift}). Unambiguous space points were then derived by looking at the delay line information and requiring the condition $T = t_{d1} + t_{d2} - 2t_d$, where T is the transit time of the full delay line, t_d is the drift time measured by the sense wires, and t_{d1}, t_{d2} are the times measured at the ends of the delay line. For every detector, we merged space points in the chamber and in the silicon, averaging by error weighting those points within 4σ . In 90% of the cases, points in a detector were found both by the chamber and the silicon. In 8% of the cases, the x coordinate was not reconstructed in the silicon (dead channels, but the y coordinate was available), while in 2% of the cases the y coordinate was not measured by the chambers but only by the silicon.

B. Geometrical alignment of the detectors and determination of the machine lattice functions

In order to define a precise trajectory with the space points measured by the detectors, the spectrometer alignment was improved relative to the survey using the data. Details of the spectrometer alignment procedure are given in Appendix B. Within the available statistics, the x coordinate scale for each detector was determined to two parts in a thousand ($70 \mu\text{m}$ over 3.5 cm); the y coordinate scale was known to within one part in 10 000. By using the simulation described in Appendix D, we derived a systematical error of $\leq 0.1\%$ on the measurement of the slope b and of the optical point $dN_{el}/dt|_{t=0}$; because these errors are correlated, the resulting system-

atical error on the total elastic rate $N_{el} = dN_{el}/dt|_{t=0}/b$ is negligible.

At $\sqrt{s}=546$ (1800), the minimum angle detected by the spectrometer was determined to within 0.48 (0.38) μrad , putting a limit of 0.07% (0.17%) on the systematical error of the extrapolation to the optical point.

The machine nominal momentum was known to within 0.12% from the measurement of the integrated field of all Tevatron magnets and from the average radius of the closed orbit given by the rf frequency value [5]; the consequent systematical errors in the determination of the slope and of the optical point are listed in Table VI. The lattice transport matrices were determined as described in Appendix C. Several $\simeq 1\%$ adjustments to the nominal Tevatron optics were made; within our statistics, the transport matrix elements were relatively adjusted to better than one part in a thousand. A systematical error of 0.15% on the absolute value of the lattice functions could not be excluded. By using the detector simulation described in Appendix D, at $\sqrt{s}=546$ (1800) we derived a systematical error of 0.1% (0.1%) for the slope value, 0.4% (0.2%) for the optical point, and 0.3% (0.3%) for the total elastic rate. At $\sqrt{s}=546$, when constraining the slope b to be $15.35 \pm 0.2 \text{ GeV}^{-2}$ (see Sec. V), the systematical errors on the optical point and on the total elastic rate were reduced to 0.2% . (All systematical errors are summarized in Table VI.)

C. Data filtering

We collected 34 552 and 38 759 elastic triggers at $\sqrt{s}=546$ and 1800, respectively (see Table II). We rejected events if any trigger counter was out of time by more than $\pm 10 \text{ ns}$ [time of flight (TOF) FILTER] in order to eliminate triggers from satellite bunches spaced by $\pm 20 \text{ ns}$ with respect to main bunches. Events lost by this cut or because of early accidental hits in the counters were evaluated by pulsing all counters during data taking to simulate elastic event triggers and counting the number of missing or rejected pulser triggers; the loss was $\simeq 1.0\%$ and is listed in Table III.

A fraction of our triggers was due to random coincidences of two beam halo particles going in opposite directions through the east and west sides of one spectrometer arm. When these halo particles, which passed on time in one side (west/east) of one spectrometer arm, were also detected at an earlier time by the drift chambers of the other spectrometer arm on the opposite side (east/west), the event was rejected. The number of events passing this filter is listed in Table II (HALO FILTER).

We then looked at the hit multiplicity in the various detectors. If $S1$ or $S2$ had more than two hits in the triggering arm and $S1 + S2$ in the other arm had three counters out of four fired and more than four y hits in any one of the silicon detectors, we rejected the event. The same requirement (HIT FILTER) was applied to $S6$ and $S7$. On the east side ($S6, S7$), this filter rejected all elastic events traveling at an angle smaller than that subtended by the detectors and interacting in the vacuum chamber

TABLE II. Analysis event flow.

	$\sqrt{s}=546$	1st run at $\sqrt{s}=1800$	2nd run at $\sqrt{s}=1800$
	Number of events		
Triggers	34 522	16 993	21 766
TOF filter	33 714	15 493	19 126
HALO filter	33 714	11 402	16 167
HIT filter	29 981	8 692	13 054
ROAD filter	28 151	6 136	8 055
Vertex cut	23 868	5 313	7 033
Collinearity cut	22 929	4 856	6 662
Fiducial cut	18 919	3 144	5 630

separating the detectors from the beam; it also rejected low mass diffractive events. On the west side ($S1, S2$), the filter rejected triggers caused by beam losses. The number of events surviving this filter is listed in Table II; the filter efficiency for retaining good events (100%) is discussed in Appendix A. Corrections for event losses due to nuclear interactions in the detectors ($\simeq 1.8 \pm 0.2\%$) were also applied, as listed in Table III and discussed in Appendix A.

In the remaining events, we used the following procedure to reconstruct the vertex coordinates (x_0, y_0) at $z=0$ and the antiproton (proton) scattering angle $\theta_{\bar{p}(p)}$. We required at least one point in both east and west sides of a spectrometer; the points on the east side ought to lie inside a $250 \mu\text{rad}$ cone around the straight line passing through the points on the west side and $x = y = 0$ at $z = 0$ (ROAD FILTER) (see Table II).

On the west side, when $S3$ and ($S1$ and/or $S2$) were present, we reconstructed the \bar{p} trajectory by determining (x_0, y_0) and $\theta_{\bar{p}}$ with Eq. (1). Then, by using (x_0, y_0) and the points measured by $S6$ and/or $S7$, θ_p was also determined with Eq. (1). When $S3$ or $S1$ and $S2$ were missing (see Table IV), we assumed $x_0 = y_0 = 0$. In cases where some detectors had more than one point (usually a δ ray in only one detector), by assuming $x_0 = y_0 = 0$, we first determined all possible combinations of points in different detectors that lay within a road. In most cases, this procedure was sufficient to reject spurious hits. For all combinations of points in different roads, we reconstructed the proton and antiproton trajectories as described above. If more than one combination was left (see Table V), we selected the one with the best collinearity.

D. Background evaluation and removal

Figure 3 shows the y_0 versus x_0 distributions for all events at $\sqrt{s} = 546$ and 1800 GeV. A 3.5σ vertex cut was applied to reduce the background contamination. Figure 4 compares collinearity ($\Delta\theta = \theta_{\bar{p}} - \theta_p$) distributions for the events accepted and for those rejected by the vertex cut. Events lost by this cut ($\leq 0.2\%$) were accounted for in the acceptance calculation. At $\sqrt{s}=546$, the collinearity distribution width, $\sigma_{\Delta\theta} = 53 \mu\text{rad}$, is mainly contributed by the beam angle spread at the interaction region; at $\sqrt{s} = 1800$, $\sigma_{\Delta\theta} = 16 \mu\text{rad}$ is well accounted for by the detector resolution and the beam angular divergence (see also Appendix D). Figure 5 shows $\Delta\theta_y$ versus $\Delta\theta_x$ collinearity plots for all events passing the vertex cut. The solid lines indicate the collinearity cut defining our final sample of elastic events; events lost by this cut ($\leq 0.2\%$) were also accounted for in the acceptance calculation. The residual background contamination ($\leq 0.5\%$, as listed in Table III) was estimated from the events with $\Delta\theta_x$ outside the dashed lines in Fig. 5; Fig. 6 shows the $\Delta\theta_y$ distribution for these events, normalized at $\Delta\theta_y$ outside the dashed line to the $\Delta\theta_y$ distribution of events inside the $|\Delta\theta_x|$ collinearity cut. The amount of background counted inside the $|\Delta\theta_y|$ collinearity cut was then statistically removed. Figure 7 shows dN/dt distributions for all events within the collinearity cut and for the removed background.

E. Beam tilt-angle determination

The angle of the beam with respect to the spectrometer axis (tilt angle) was determined using the data. In

TABLE III. Corrections (%).

	$\sqrt{s}=546$	1st run at $\sqrt{s}=1800$	2nd run at $\sqrt{s}=1800$
	arm 0/arm 1	arm 0/1	arm 0/1
Background	-0.3/ -2.2	-0.37/ -0.85	-0.28/ -0.14
TOF losses	+1.1/ +1.65	+1.5/ +1.8	+1.7/ +0.9
Nuclear interactions	+1.8	+1.8	+1.8
Slope change	+0.78	0	0
at $-t > 0.1 \text{ GeV}^2$ ^a			

^aThis correction was applied only to the total elastic rate.

TABLE IV. Elastic events (%).

Reconstructed with	$\sqrt{s}=546$	$\sqrt{s}=1800$
5 detectors	95.33	95.25
4 detectors ^a	4.60	4.70
3 detectors	0.07	0.05
2 detectors	0.00	0.00

^a3.0 are due to nuclear interactions in front of $S1$, $S2$, $S6$, and $S7$.

the y - z plane, where the spectrometer covers negative and positive angles around $\theta_y = 0$, we adjusted the spectrometer by an angular tilt equal to the mean value of the θ_y distribution. In the x - z plane the spectrometer did not cover the angular region around $\theta_x = 0$. In order to determine the tilt angle, we calculated the spectrometer acceptance for several angles of the beam with respect to the spectrometer axis (see Appendix D for a description of the simulation). For each tilt angle, we fitted the t distribution of the data corrected by the corresponding acceptance, independently for arm 0 and arm 1, with the form $\frac{dN_{el}}{dt} |_{t=0} e^{bt}$. We adjusted the spectrometer by the tilt angle that minimized the differences between the $\frac{dN_{el}}{dt} |_{t=0}$ and b values determined by the fits in the two spectrometer arms. As shown in Fig. 8, the values of b , $dN_{el}/dt |_{t=0}$, and N_{el} do not depend on the beam tilt angle when fitting both arms simultaneously. As a check, once we adjusted the tilt angle, we selected all events with $|\theta_y| \leq 400 \mu\text{rad}$ and, after correcting for acceptance, we fit the $dN_{el}/d\theta_x$ distribution with the form $K e^{-b(\theta_x - \theta_0)^2}$ and verified that the tilt angle θ_0 from the fit was consistent with zero within $1.0 \mu\text{rad}$.

IV. DATA FITTING

In order to avoid edge effects, we removed events which lay within 0.5 mm of fully efficient detector boundaries; the spectrometer t acceptance was accordingly calculated with the full simulation described in Appendix D. The t distribution of the data, corrected for acceptance, was fit with the exponential form $A e^{bt}$, with $A = L \frac{d\sigma_{el}}{dt} |_{t=0}$; an exponential t dependence is expected for a nucleon density with Gaussian distribution [6]. This fit functional

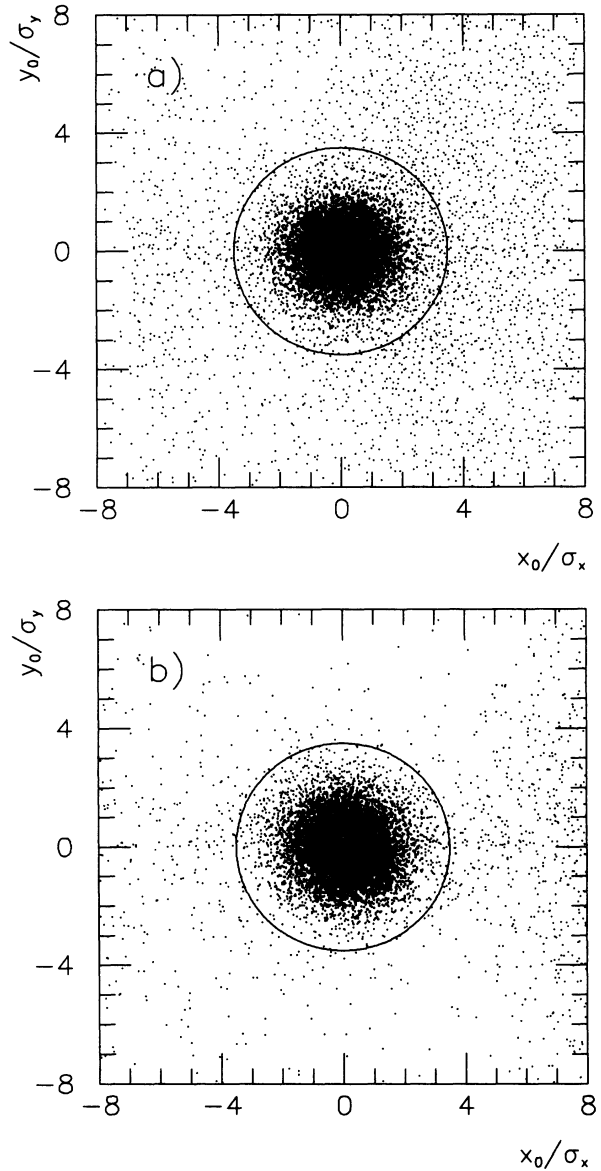


FIG. 3. Interaction point distributions in the transverse plane at $z = 0$ for (a) $\sqrt{s}=546$ and (b) $\sqrt{s}=1800$ GeV, in units of the reconstruction errors $\sigma_{x(y)}$ ($\simeq 350 \mu\text{m}$). The circle indicates the vertex cut.

TABLE V. Elastic events (%).

Number of reconstructed elastic combinations	Number of detectors with more than one hit					
	0	1	2	3	4	5
At $\sqrt{s}=546$						
1	80.05	14.43	1.68	0.21	0.11	0.85
2		1.35	0.41	0.06	0.07	0.14
3		0.32	0.12	0.02	0.01	0.01
> 3		0.01	0.11	0.01	0.02	0.01
At $\sqrt{s}=1800$						
1	76.87	16.97	2.36	0.28	0.03	
2		1.53	0.48	0.12	0.01	0.01
3		0.39	0.17	0.05	0.00	
> 3		0.21	0.49	0.02	0.01	

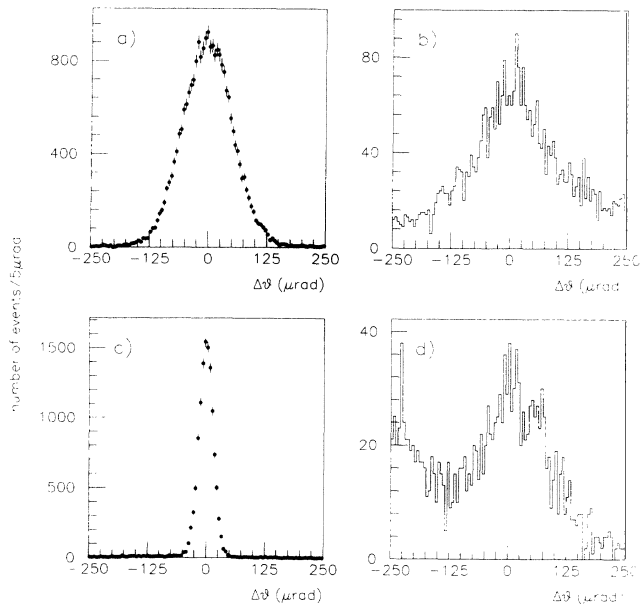


FIG. 4. Collinearity ($\Delta\theta = \theta^p - \theta^P$) distributions for (a) events accepted and (b) events rejected by the vertex cut at $\sqrt{s}=546$; (c) and (d) are the corresponding distributions at $\sqrt{s}=1800$ GeV.

form was corrected for the Coulomb scattering contribution [7],

$$1 + \frac{4\pi\alpha^2(\hbar c)^2 G^4(t)}{A|t|^2} e^{b|t|} + \frac{\alpha(\rho - \alpha\Phi)\sigma_T G^2(t)}{A|t|} e^{b|t|/2},$$

where the nucleon form factor was parametrized as $G(t) = [1 + |t|/(0.71 \text{ GeV}^2)]^{-2}$ and the relative phase as $\Phi(t) = -0.577 + \ln(k|t|^{-1})$, α is the fine structure constant, σ_T the total cross section [2], and $k = 0.08$ (0.07) GeV^2 at $\sqrt{s} = 546$ (1800) GeV . Having set the ratio of the real to imaginary part of the nuclear elastic scattering $\rho = 0.15$ [9,10], the correction for the Coulomb scattering contribution is $\simeq 1.0\%$ at the lowest t . At $\sqrt{s} = 1800$, the spectrometer t resolution [$\sigma_t \simeq 0.009 \text{ GeV} (\sqrt{-t})$] was smaller than the $\Delta t = 0.01 \text{ GeV}^2$ bin width used in the fit and no smearing was applied when fitting the observed t distribution. At $\sqrt{s} = 546$, where $\sigma_t \simeq 0.019 \text{ GeV} (\sqrt{-t})$ was comparable to the $\Delta t = 0.004 \text{ GeV}^2$ bin width used in the fit, smearing corrections ($\simeq 0.3\%$) were applied by fitting the functional form $A[1 - b(0.019 \text{ GeV})^2/2]e^{bt[1 - b(0.019 \text{ GeV})^2/2]}$.

Fits at $\sqrt{s} = 546$ and 1800 GeV are shown in Fig. 9.

At $\sqrt{s} = 1800$, the beam angular divergence was small and consequently the spectrometer acceptance for detecting elastic recoils was 100% over a wide (θ_x, θ_y) region. As a check, we fitted the data in this region with the form $Ae^{-b\rho^2(\theta_x^2 + \theta_y^2)}$. This fit yielded A and b values consistent within 0.5% with the results obtained by fitting the acceptance-corrected t distribution of all events.

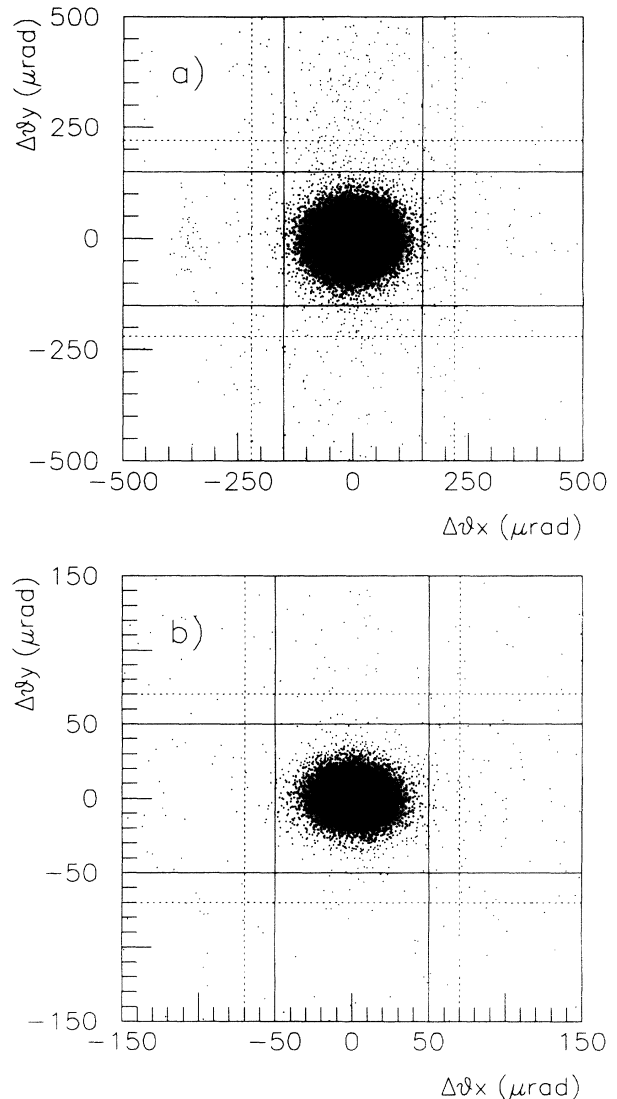


FIG. 5. Collinearity distributions ($\Delta\theta_y = \theta_y^p - \theta_y^P$ vs $\Delta\theta_x = \theta_x^p - \theta_x^P$) for events accepted by the vertex cut at (a) $\sqrt{s}=546$ and at (b) $\sqrt{s}=1800$ GeV . The solid lines indicate our collinearity cuts; events with $\Delta\theta_x$ outside the dashed lines are used to estimate the background contamination inside the collinearity cuts.

V. RESULTS AND CONCLUSIONS

At $\sqrt{s} = 546$, our value of the elastic slope $b = 15.28 \pm 0.58$ (± 0.09 syst.) GeV^{-2} in the range $0.025 < -t < 0.08 \text{ GeV}^2$ is in good agreement with UA4 value $b = 15.3 \pm 0.3 \text{ GeV}^{-2}$ at $|t| < 0.1 \text{ GeV}^2$ [8] and with the recent UA4/2 result $b = 15.4 \pm 0.2 \text{ GeV}^{-2}$ in the range $0.00075 < -t < 0.12 \text{ GeV}^2$ [9]. In order to improve our errors on the optical point and on the total number of elastic events, we made use of these more accurate measurements of the slope by refitting our data with the additional constraint that the slope be $15.35 \pm 0.20 \text{ GeV}^{-2}$ (average of the UA4 and UA4/2 results). We obtain

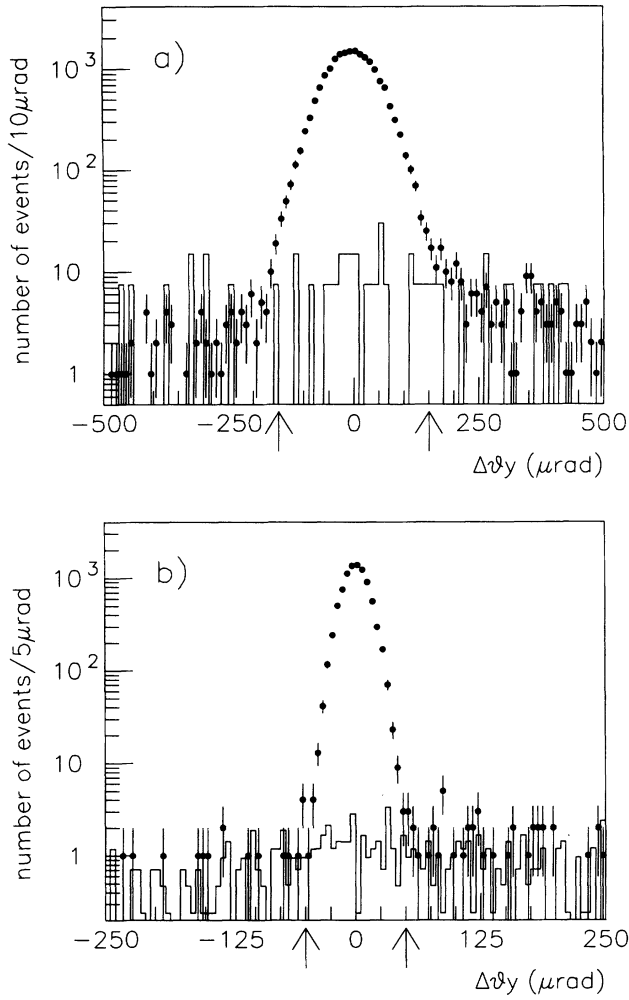


FIG. 6. Collinearity ($\Delta\theta_y = \theta_y^{\bar{p}} - \theta_y^p$) distributions at (a) $\sqrt{s}=546$ and at (b) $\sqrt{s}=1800$ GeV. The collinearity resolution $\sigma_{\Delta\theta_y}$ is $\simeq 53$ (16) μrad at $\sqrt{s}=546$ (1800). (•) Events that passed the vertex and the $3\sigma_{\Delta\theta_x}$ collinearity cuts. (—) Background events that passed the vertex cut but have $|\Delta\theta_x| > 4\sigma_{\Delta\theta_x}$, normalized to the number of events with $|\Delta\theta_y| > 4\sigma_{\Delta\theta_y}$. Arrows indicate the $\Delta\theta_y$ collinearity cut.

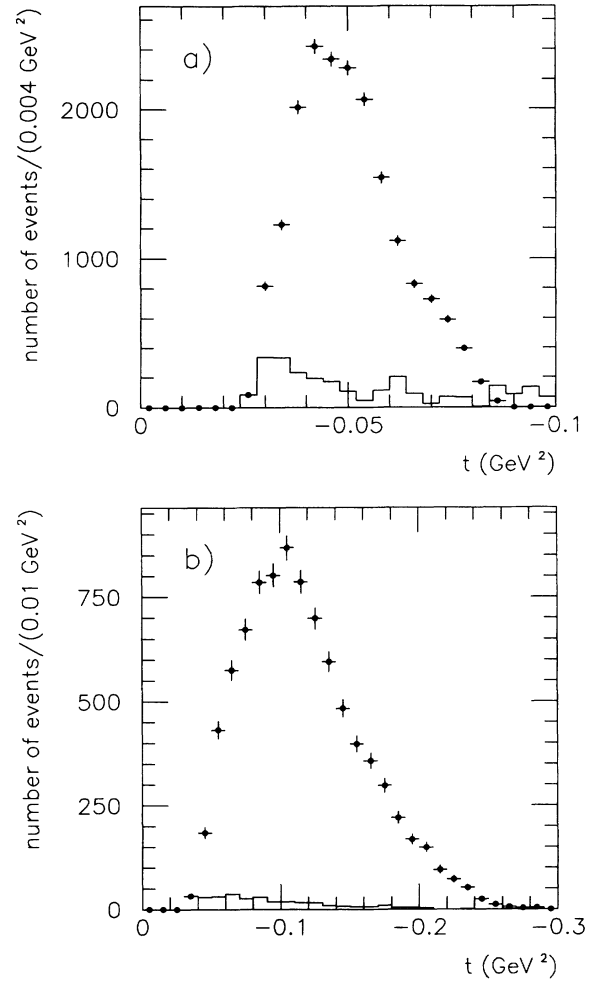


FIG. 7. t distributions for events passing all cuts (•) at (a) $\sqrt{s}=546$ and at (b) $\sqrt{s}=1800$ GeV. The t distribution of background events passing all cuts (—) is amplified by a factor 10.

TABLE VI. Sources of systematical errors (%).

	$\sqrt{s}=546$			$\sqrt{s}=1800$		
	A	b	N_{el}	A	b	N_{el}
Vertex cut	0.2		0.2	0.2		0.2
TOF losses	0.2		0.2	0.2		0.2
Background	0.2		0.2	0.2		0.2
Magnetic lattice	0.2	0.1	0.2	0.1	0.2	0.3
t_{min}	0.07		0.07	0.17		0.17
x scale	0.1	0.1		0.1	0.1	
Tilt angle	0.07	0.05	0.05	0.2	0.07	0.15
Nuclear interactions	0.2		0.2	0.2		0.2
Beam momentum	0.24	0.24		0.24	0.24	
b at $-t > 0.25$ GeV ²						0.2
Total	0.52	0.26	0.45	0.48	0.32	0.54

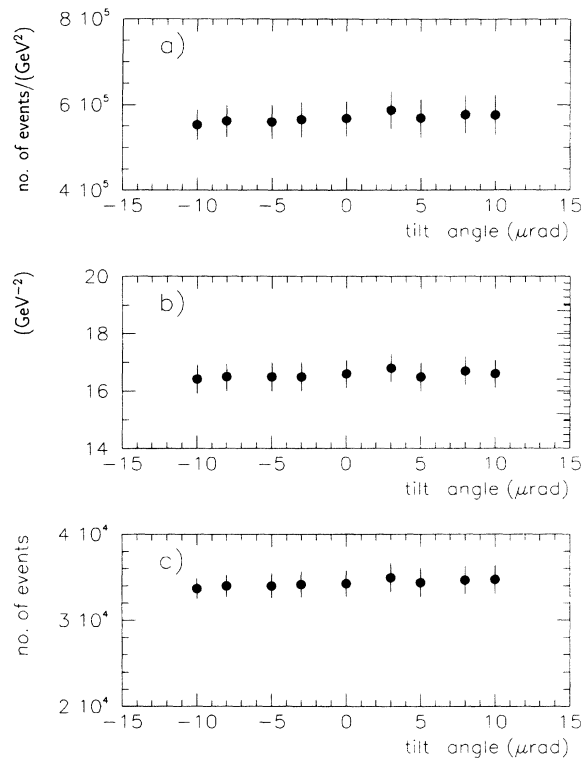


FIG. 8. Results of simultaneous fits to the data t distributions measured by the spectrometer arm 0 and arm 1 as a function of the beam angle with respect to the spectrometer axis (tilt angle). For each tilt angle, t distributions were corrected for the corresponding acceptance. Data are from the second run at $\sqrt{s}=1800$. (a) Optical point $\frac{dN_{el}}{dt} |_{t=0}$; (b) slope b ; (c) number of elastic events N_{el} .

$b = 15.35 \pm 0.19 \text{ GeV}^{-2}$. At the same energy, the total number of elastic events, $dN_{el}/dt |_{t=0} / b$, was also corrected by 0.78% to account for changes of the slope at $-t \geq 0.1 \text{ GeV}^2$ as listed in Ref. [8].

At $\sqrt{s} = 1800$, similar changes of the slope (i.e., $b = 15.0 \text{ GeV}^{-2}$ at $-t \geq 0.25 \text{ GeV}^2$) would produce a 0.2% change of the total number of elastic events, which

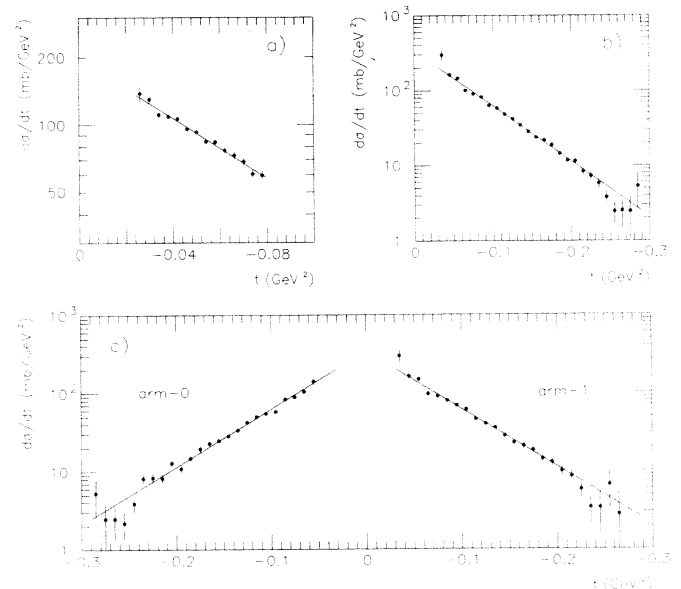


FIG. 9. Differential cross section of proton-antiproton elastic scattering at (a) $\sqrt{s}=546 \text{ GeV}$ and at (b) $\sqrt{s}=1800 \text{ GeV}$; (c): differential cross section measured by each spectrometer arm at $\sqrt{s}=1800 \text{ GeV}$. Lines represent the fit results described in the text.

was taken as a systematical error on the total number of elastic events at $\sqrt{s} = 1800$ due to our limited t range. All systematical errors are summarized in Table VI.

At $\sqrt{s} = 1800$, our measurement of the elastic slope $b = 16.98 \pm 0.25 \text{ GeV}^{-2}$ (0.24 GeV^{-2} statistical and 0.05 GeV^{-2} systematical) in the range $0.04 < -t < 0.29 \text{ GeV}^2$ improves by a factor of 2 the accuracy of the E710 measurement $b = 16.99 \pm 0.47 \text{ GeV}^{-2}$ in the range $0.001 < -t < 0.143 \text{ GeV}^2$ [10]. By making use of our measurement of the luminosity [2], we determine the total elastic scattering cross section to be $\sigma_{el} = 12.87 \pm 0.30$ (19.70 ± 0.85) mb at $\sqrt{s} = 546$ (1800) GeV. Results are listed in Table VII. Our results on the slope parameter and the total elastic cross section are presented in Fig. 10 together with other $\bar{p}p$ experiments in the

TABLE VII. Results.

	$\sqrt{s}=546$	$\sqrt{s}=1800$
	Fit results	
$b \text{ (GeV}^{-2}\text{)}$	15.35 ± 0.18	16.98 ± 0.24
$A \text{ (GeV}^{-2}\text{)}$	$4\,043\,598 \pm 48\,558$	$1\,336\,532 \pm 40\,719$
(A, b) covariance	0.79	0.93
χ^2	13.06	60.96
N_{DF}	13	46
χ^2/N_{DF}	1.01	1.32
	Final results (systematical errors included)	
$L \text{ (mb}^{-1}\text{)}^a$	$20\,624 \pm 2.1\%$	$3994 \pm 2.9\%$
$b \text{ (GeV}^{-2}\text{)}$	15.35 ± 0.19	16.98 ± 0.25
$A \text{ (GeV}^{-2}\text{)}$	$4\,043\,598 \pm 52\,915$	$1\,336\,532 \pm 40\,943$
Elastic rate	$265\,535 \pm 2411$	$78\,691 \pm 1463$
$\sigma_{el} \text{ (mb)}$	12.87 ± 0.30	19.70 ± 0.85
$\frac{d\sigma_{el}}{dt} _{t=0} \text{ (mb GeV}^{-2}\text{)}$	196.1 ± 6.0	334.6 ± 18.8

^aReference [2].

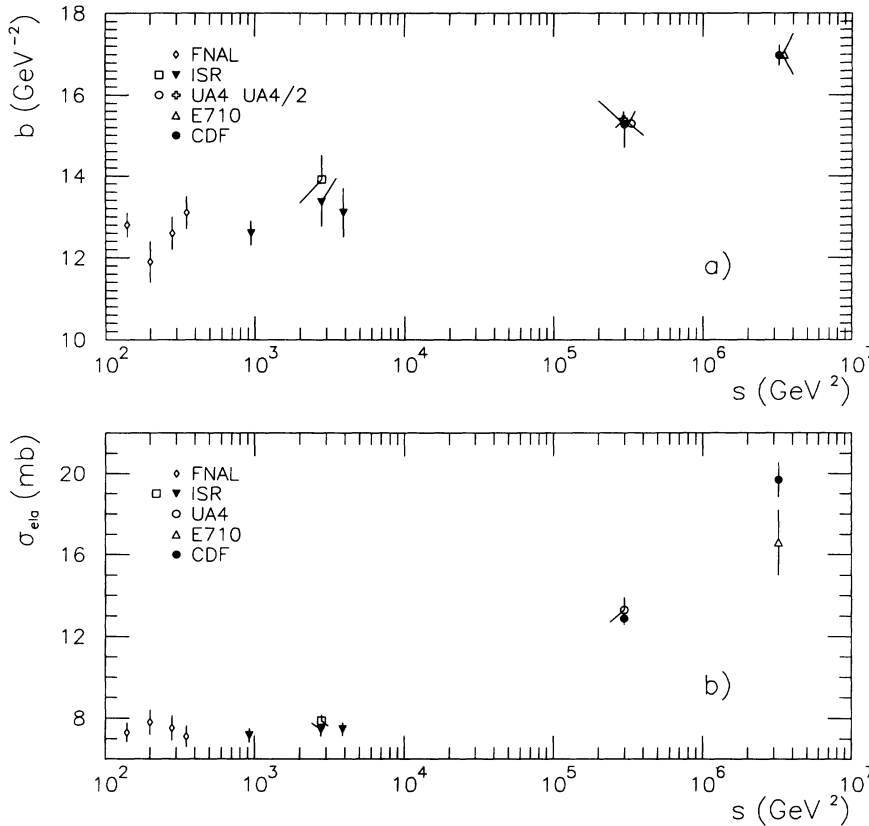


FIG. 10. Our results for (a) the slope b and (b) the total elastic cross section compared to other proton-antiproton experiments in a similar t range ($-t \leq 0.1 \text{ GeV}^2$): FNAL, Ref. [11]; ISR, Ref. [12]; UA4, Ref. [8]; UA4/2, Ref. [9]; E710, Ref. [10].

same t range. Assuming an s dependence of the slope $b = b_0 + 2\alpha' \ln(s/s_0)$, the data at $\sqrt{s} = 546$ and 1800 GeV yield $\alpha' = 0.34 \pm 0.07 \text{ GeV}^{-2}$. A fit including also the data from the CERN Intersecting Storage Rings (ISR) in Fig. 10 yields $\alpha' = 0.26 \pm 0.02 \text{ GeV}^{-2}$.

ACKNOWLEDGMENTS

We thank the Fermilab Accelerator Division for the construction and operation of the Tevatron and of the Antiproton Source. In particular, we feel indebted to D. Finley, N. Gelfand, H. Jostlein, and K. Koepke for many useful suggestions. We wish to thank the Fermilab Computer division, the technical staff of the Collider Detector at Fermilab (CDF) and of the collaborating Institutions for their contribution to the construction and operation of CDF. The dedicated effort of the many technicians and engineers at Frascati and Rockefeller, who contributed to the design, construction, and installation of the spectrometer and of the forward tracking vertex detectors, is warmly acknowledged; we especially thank M. Biagioli, G. Bisogni, A. Ceccarelli, M. DiVirgilio, G. Fontana, R. Heidecker, D. Humbert, E. Iacuessa, P. Locchi, A. Rutili, G. Sensolini, D. Sceanovich, and M. Troiani. We are grateful to G. Tonelli and E. Focardi who led the construction of our silicon detectors. This work was supported by the Department of Energy, the National Science Foundation, the Istituto Nazionale di Fisica Nucleare, and the Ministry of Science, Culture and Education of Japan.

APPENDIX A: CHECKS OF DETECTOR EFFICIENCY

1. Counter efficiency

The trigger for elastic events required the coincidence of all ten scintillation counters in each arm. We checked the trigger efficiency with the data by selecting, in inelastic and diffractive trigger events [1,2], single tracks detected by the chamber and the silicon in every detector $S1$, $S2$, $S3$, $S6$, and $S7$. We collected about 7500 such tracks in every run. For all tracks, the two counters sandwiching the tracking detectors always had an analogue to digital converter (ADC) pulse height consistent with a minimum ionizing particle. For every run, the counter efficiency was found to be larger than 99.99%. By looking at the time to digital converter (TDC) information, we determined that the trigger lost about 1.0% of the events, consistent with the pulser corrections (TOF losses) listed in Table III.

2. Efficiency of tracking detectors and of filters

Table IV shows a negligible uncorrelated probability of losing a good event because of tracking detector inefficiencies. Our analysis resolved all multihit events. We studied our analysis filters as the only possible cause of inefficiency. The TOF filter used a conservative cut, as shown in Fig. 11. The HALO filter was harmless, since

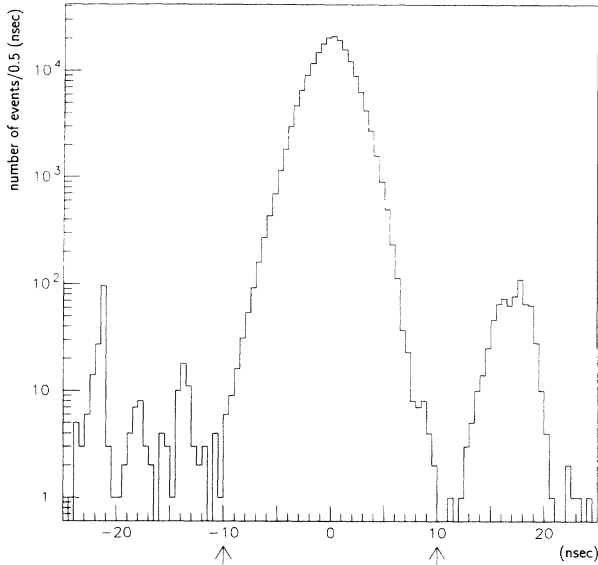


FIG. 11. Time of flight distribution of all trigger counters at $\sqrt{s}=1800$ GeV. The $\bar{p}p$ bunches interact at $t = 0 \pm 1$ ns; arrows indicate the TOF filter cut.

it removed identified beam halo events. From the known rate of beam splashes in the detectors, we estimated that the hit multiplicity filter would lose 0.1% of good events overlapped by random splashes of beam particles. We first analyzed those events rejected because of high multiplicity in $S6$ and $S7$. By using $S1$, $S2$, and $S3$ points, we projected the antiproton track into $S6$; the projected point would be the impact point of the elastically scattered proton if the event was elastic. Figure 12 shows the y versus x distribution of the projected impact points in $S6$. Indeed, 73% of the rejected events point to the beam pipe and can be attributed to elastic events out of acceptance. Of the remaining 27% of these events, 18% project inside the detectors and 9% inside the vacuum chamber. In each of the two regions, these events correspond to 3.3% of the elastic events or 15% of the single diffraction proton dissociation events. We investigated the single diffraction hypothesis. In our diffractive analysis [1], we determined that 20% of the single proton diffraction dissociation cross section is at *low masses* ($M^2 < 6$ GeV²); these masses have predominant 2- and 3-body decays. The decay products, at very small angle with respect to the beam, are likely candidates to produce nuclear interactions in the beam pipe in front of $S6$. We know from our simulation [2] that 36% of the *low mass* events should also be detected by our inelastic vertex detector around the interaction region and, in fact, $40 \pm 6\%$ of the remaining 27% of the events rejected by the hit filter were detected. For events rejected by the multiplicity filter in $S1$ and $S2$, we looked at the collinearity distribution using $S3$, $S6$, and $S7$ (Fig. 13). The comparison with the collinearity distribution of good events shows that $\simeq 0.1\%$ of good elastic events could at most have been rejected, in agreement with the estimated probability of a beam splash overlapping a good event.

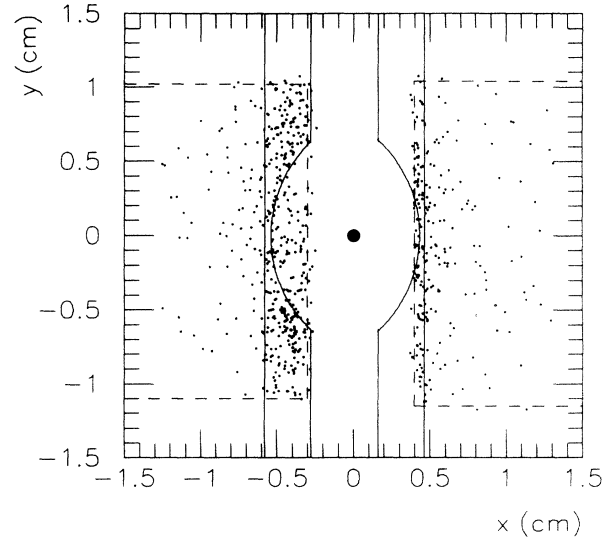


FIG. 12. Impact point distribution obtained by projecting the antiproton tracks onto detector $S6$ (on the proton side) for events rejected because of many hits in $S6 + S7$ (HIT FILTER) at $\sqrt{s}=1800$ GeV. The solid line indicates the beam pipe; (---) acceptance of the antiproton detectors projected in $S6$; (•) beam position.

3. Event losses due to nuclear interactions in the detectors

Given the thickness of the components of a detector, nuclear interaction losses in each detector were calculated to be $\simeq 1.4\%$. As this correction is not negligible, we checked it using our data. By looking at events which had a single track in the $S2$ ($S6$) detector but more than one track in the following $S1$ ($S7$) detector, we determine

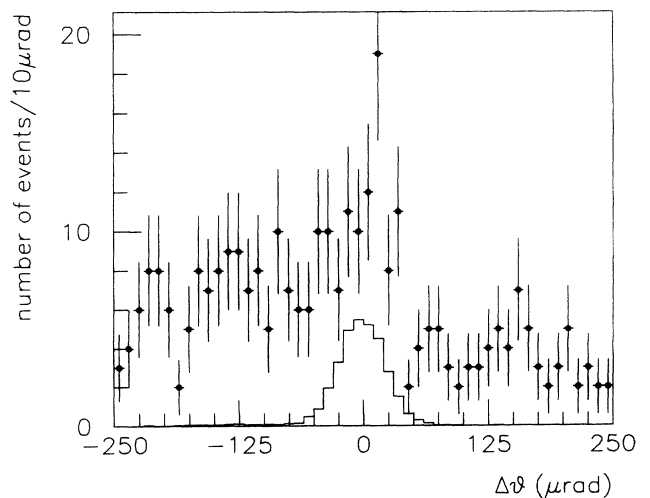


FIG. 13. Collinearity ($\Delta\theta = \theta^{\bar{p}} - \theta^p$) distribution (•) for events rejected because of large multiplicities in $S1 + S2$ (HIT FILTER) in all the data (corresponding to 27 693 good elastic events), after the fiducial and vertex cuts. The solid line shows the collinearity distribution of elastic events.

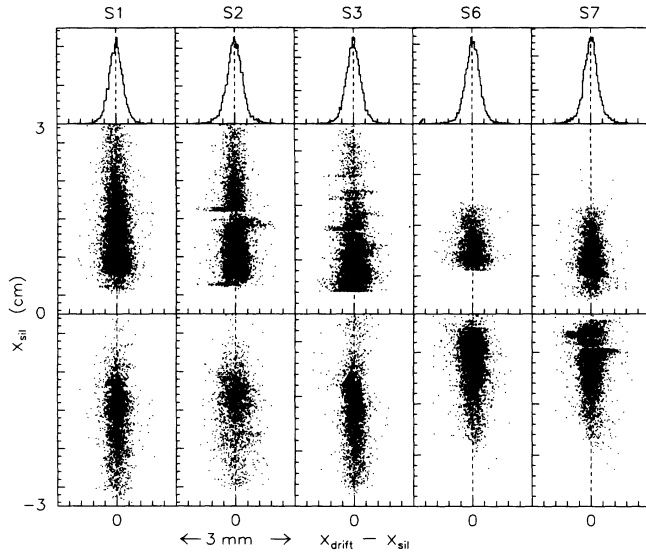


FIG. 14. Distribution of the difference between the x coordinate measured by the drift chamber (x_{drift}) and by the silicon (x_{sil}) vs x_{sil} for each spectrometer detector at $\sqrt{s}=1800$ GeV.

the nuclear loss correction to be $1.2\% \pm 0.1\%$ on the basis of 750 interactions observed in all our data. When the interaction occurred at the end of $S2$ ($S6$), hits were always observed in the $S1$ ($S7$) detector of the opposite arm; the opposite side was clean when the interaction occurred in $S1$ ($S7$). In this last category of events, by projecting from $S2$, $S3$, and $S6$ into $S1$ and $S7$, we determined a 45% probability of still finding a track in the right position when a nuclear interaction occurred. These two observations allowed the precise determination of the nuclear interaction losses for elastic and diffractive scattering, as listed in Table III.

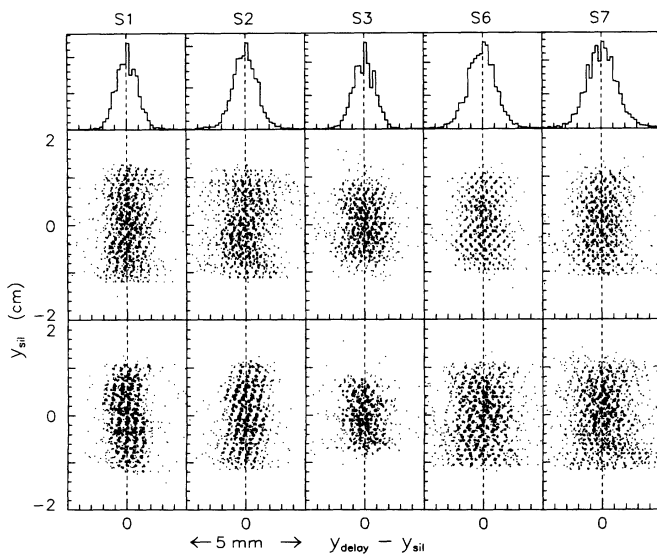


FIG. 15. Distribution of the difference between the y coordinate measured by the delay line (y_{delay}) and by the silicon (y_{sil}) vs y_{sil} for each spectrometer detector at $\sqrt{s}=1800$ GeV.

APPENDIX B: GEOMETRICAL ALIGNMENT OF THE SPECTROMETER

The vertical and horizontal coordinate scales were determined by the silicon detector pads and strips, lithographically produced with an accuracy of a few micrometers over 3.5 cm. For events with only one hit in a given detector, we adjusted the chamber drift velocity by minimizing $(x_{\text{drift}} - x_{\text{sil}})$ versus x_{sil} (Fig. 14). The same procedure was used for the delay lines, which required nonlinear corrections at both y ends of the detector (Fig. 15). Since the silicon pads had better y resolution than the chambers and were fully efficient, the y coordinate was determined by the silicon. The y coordinate scale was known to better than one part in 10 000 (accuracy of the lithographic mask). On the contrary, the x coordinate was determined by the chambers, which had better x resolution. Within the available statistics, the absolute x scale for each detector was determined in two parts in a thousand ($70 \mu\text{m}$ over 3.5 cm). Since the elastic scattering angle was determined by all detectors, the error on the θ_x scale was reduced to less than one part in a thousand.

In order to reduce the error on the x and y positions of each detector resulting from the survey, we selected events with only one hit in every detector (hits ought to be within a few millimeters from a straight line fit); assuming that these events originated at $x = y = z = 0$, by using Eq. (1) we projected all points in $S3$ into the other four detectors and corrected for the x and y offsets of each detector by subtracting the mean value of the distribution of the differences between the measured and projected coordinates.

Within the statistics, the detectors of each arm were aligned to within $3.0 \mu\text{m}$, as shown in Fig. 16. As a by-product, we determined the detector resolutions quoted in Sec. II and used in the simulation. Figure 17 shows distributions of the difference between the coordinates as measured by $S2$ ($S6$) and as projected into $S2$ ($S6$) by using $S1$, $S3$, and $S7$, for elastic events selected by $S1$, $S3$, and $S7$ only. As shown from the comparison with simulated events, detector resolutions have a Gaussian distribution; therefore, non-Gaussian tails in collinearity distributions could only be attributed to background.

Once we aligned independently the two spectrometer arms, we determined the horizontal angle between them by minimizing the sum $\sum_{i=1}^5 (\Delta d_i)^2$, where Δd_i is the difference between the surveyed and actual distance d_i between two detectors in different arms at a given z_i position. After minimization, the standard deviation of Δd_i was about $70 \mu\text{m}$, consistent with the survey error; as a consequence, a systematical error of $[\sum_{i=1}^5 (\frac{L_i^h}{50 \mu\text{m}})^2]^{-\frac{1}{2}} = 1.2 (0.5) \mu\text{rad}$ was estimated on the minimum angle detected by the spectrometer at $\sqrt{s} = 546$ (1800) GeV.

A second method, independent of the survey, was used to determine the angle between the two spectrometer arms. In single diffraction events [1], recoil antiprotons with momentum smaller than $\sqrt{s}/2$ were selected which, bent by the dipole string, passed through $S1$ and $S2$ in

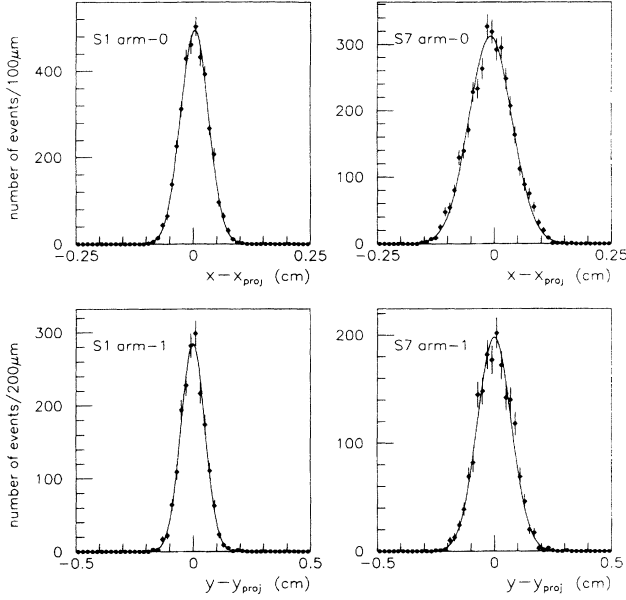


FIG. 16. Typical distributions of the difference between the coordinate measured by detectors $S1$ and $S7$ and the projected value, calculated using the coordinates measured by $S3$ and assuming the interaction point to be at $(x, y, z) = (0, 0, 0)$. The data are at $\sqrt{s} = 1800$. The distribution mean values have been adjusted to the offsets ($\approx 20 \mu\text{m}$) predicted by the simulation when assuming a pointlike interaction region. Solid lines represent Gaussian fits to the distributions.

arm 1 and through $S3$ in either arm. The recoils were projected from $S1$ and $S2$ into $S3$ assuming $x = y = 0$ at $z = 0$. From the mean value of the distribution of the difference between the measured and projected x coordinates in $S3$, we determined that the distance between

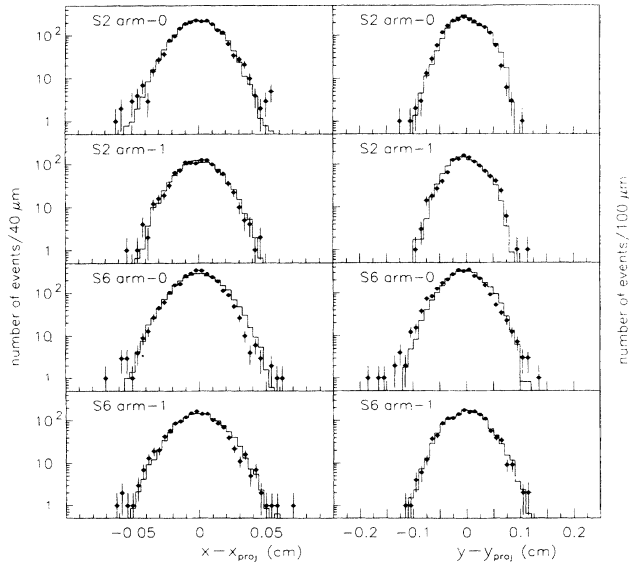


FIG. 17. Distributions of the difference between the coordinate measured by detectors $S2$ and $S6$ and the projected value, calculated using the coordinates measured by $S1$, $S3$, and $S7$. (\bullet) Data are at $\sqrt{s} = 1800$ GeV; (—) equal number of simulated elastic events.

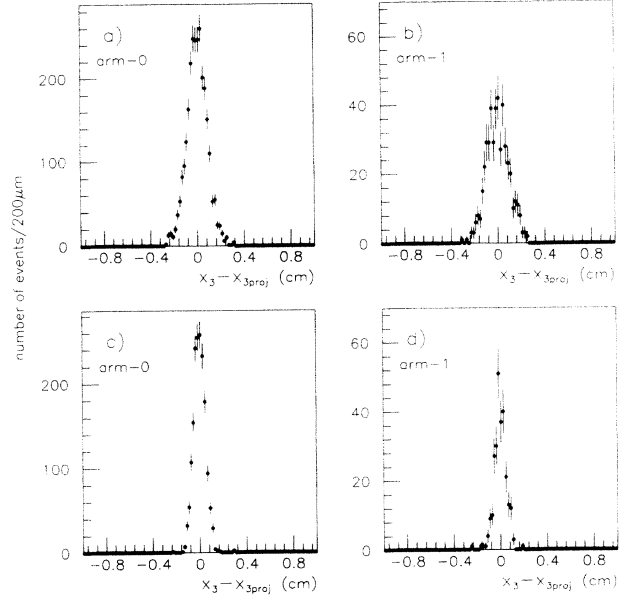


FIG. 18. Distributions of the difference between the coordinate measured by the detector $S3$ and the projected value, calculated using the coordinates measured by $S1$, $S2$ and assuming the interaction point at $(x, y, z) = (0, 0, 0)$ for the recoil antiproton in single diffraction events. $S1$ and $S2$ are always in arm 1, while $S3$ is in arm 0 or arm 1 depending on the recoil momentum and angle. (a), (b) $\sqrt{s} = 546$ GeV; (c), (d) $\sqrt{s} = 1800$ GeV.

the two spectrometer arms in $S3$ should be corrected by $2.0 \pm 40.0 \mu\text{m}$ and $-1.0 \pm 30 \mu\text{m}$ at $\sqrt{s} = 546$ and 1800 GeV, respectively (see Fig. 18). At $\sqrt{s} = 546$ (1800), the two methods described above set a limit of 0.48 (0.36) μrad on the systematical error in the determination of the minimum angle detected by the spectrometer.

APPENDIX C: STUDY OF THE TEVATRON MAGNETIC LATTICE

1. $\sqrt{s} = 1800$ GeV

At $\sqrt{s} = 1800$, only the quadrupole magnets q_1 and q_2 were powered on the spectrometer west side. Assuming that all elastic events came from $x = y = z = 0$ and using Eq. (1), we projected the impact point of an elastic recoil scattered at an angle θ from $S3$ into $S2$ as follows:

$$x_{2 \text{ proj}} = \frac{L_2^h}{L_3^h} x_3, \quad y_{2 \text{ proj}} = \frac{L_2^v}{L_3^v} y_3.$$

We then studied the differences between the projected and measured coordinates in $S2$ versus the measured coordinates in $S3$ for all events, since wrong ratios of the focal lengths $R_{h(v)} = L_2^{h(v)}/L_3^{h(v)}$ would produce a distortion

$$\delta x(y) = x(y)_2 - x(y)_{2 \text{ proj}} = \delta R_{h(v)} x(y)_3$$

where $\delta R_{h(v)}$ is the error in $R_{h(v)}$. Figure 19 shows the mean of the $\delta x(y)$ distributions as a function of $x(y)_3$ from the data and simulation; distortions at the boundaries of the $S3$ detector are due to the detector acceptance. The data and, as a check, an equal number of simulated events were fitted with the form $\delta R_{h(v)}x(y)_3$. For the data the quadrupole magnetic strength was changed until $\delta R_{h(v)}$ was found null within our sensitivity. This was achieved by adjusting the q_2 nominal magnetic strength by 2%. Since on the east side the magnet q_2 is behind the $S6$ and $S7$ detectors, the nominal optics was not changed on this side. The lattice functions were verified by projecting tracks from the west into the east side. We assigned a 0.48% error to the determination of δR_h , of which 0.12% is statistical, 0.22% is due to our systematical error on the x scale, and the rest was es-

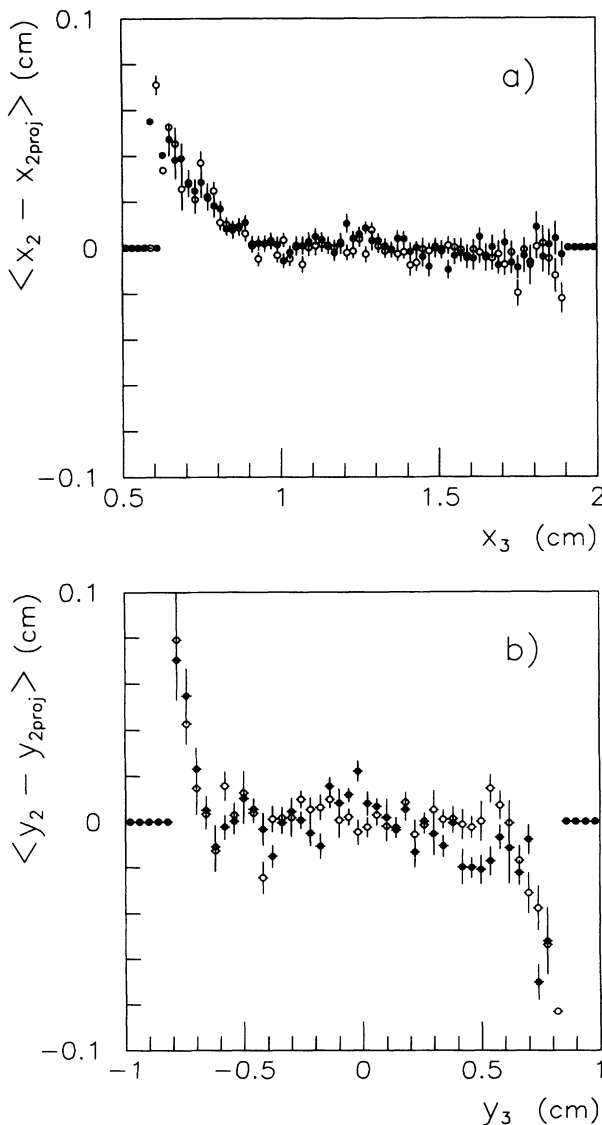


FIG. 19. Mean value of the difference between the coordinate measured by $S2$ and the projected value, calculated using the coordinate measured by $S3$ and assuming the interaction point at $(x, y, z) = (0, 0, 0)$, as a function of the coordinate measured by $S3$. (a) x coordinate and (b) y coordinate for (●) data at $\sqrt{s} = 1800$ GeV and (○) simulation.

timated by changing the fit region. The error on δR_v was 0.7%, of which 0.2% was statistical and the rest was due to the discrete structure of the y coordinate and the sensitivity to the fit region. As shown in Fig. 20, the ratios R_h and R_v behave differently for changes of the quadrupole strengths and therefore allow the determination of the q_1 magnetic strength; the uncertainties on $R_{h(v)}$ contribute a 1.0% error in the determination of the q_1 magnetic strength. By changing q_1 by this amount, the focal lengths in $S3$ and $S6$ change by 0.15% in the horizontal plane and by -0.2% in the vertical plane. Inserting these focal length changes in the simulation, we derived a systematical error of 0.2% in the determination of the optical point, 0.1% on the elastic slope, and 0.3% on the total elastic rate.

2. $\sqrt{s} = 546$ GeV

At $\sqrt{s} = 546$, the Tevatron magnetic field was reduced by a factor of 3. We first took test data with the q_0 magnetic string powered off; we repeated the above-described procedure and verified that remnant field distortions in q_1 and q_2 were not appreciable. During the data taking, the quadrupole magnets q_0 were also powered. We repeated the previous study by changing the strength of all q_0 quadrupoles by the same amount.

This time the distortion was defined as

$$\delta x(y) = x(y)_3 - x(y)_{proj} = \delta R_{h(v)} x(y)_2$$

where $R_{h(v)} = \frac{L_3^{h(v)}}{L_2^{h(v)}}$. The q_0 's strength was adjusted by

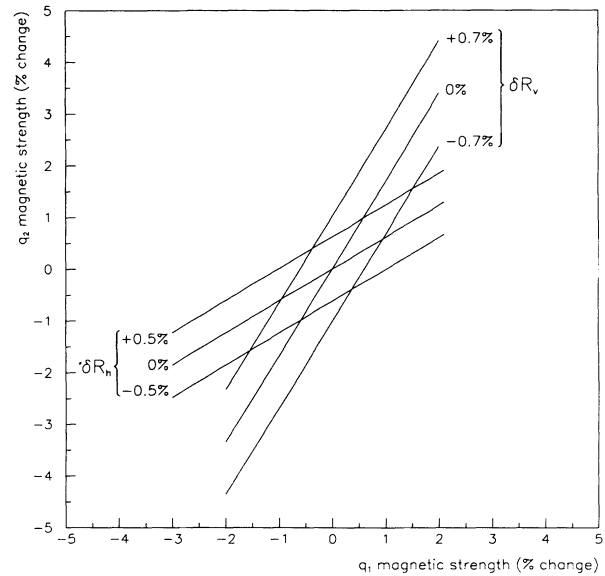


FIG. 20. Isometric lines δR_h and δR_v in the (q_1, q_2) plane. The strengths of the quadrupole magnets q_1 and q_2 determine the vertical and horizontal focal lengths $L_{2(3)}^{v(h)}$ at $S2$ and $S3$; $\delta R_{v(h)}$ is the percentage change of the ratio $R_{v(h)} = \frac{L_2^{v(h)}}{L_3^{v(h)}}$ as a function of the percentage change of the quadrupole magnetic strength. Lines are shown for the best determination of $R_{v(h)}$ and for the estimated errors. The intersection of the isometric lines corresponding to the δR_v and δR_h errors determines the uncertainty (1%) on the quadrupole magnetic strength at $\sqrt{s} = 1800$ GeV.

0.8%. The uncertainty on δR_h was estimated to be 0.48% (Fig. 21), while δR_v could not be determined to better than 4.0% because of the limited y range covered by $S2$. As shown in Fig. 22, the $\delta R_{h(v)}$ accuracy corresponds to an uncertainty on the q_0 's strength of 0.2%. By changing the q_0 's strength by such an amount in the simulation, we derived a systematic error of 0.4% in the determination of the optical point, 0.1% on the slope, and 0.4% on the total elastic rate.

3. Determination of the beam position with respect to the center of the Tevatron magnetic lattice

The spectrometer detectors were surveyed with respect to the Tevatron magnetic axis with an accuracy of 0.1

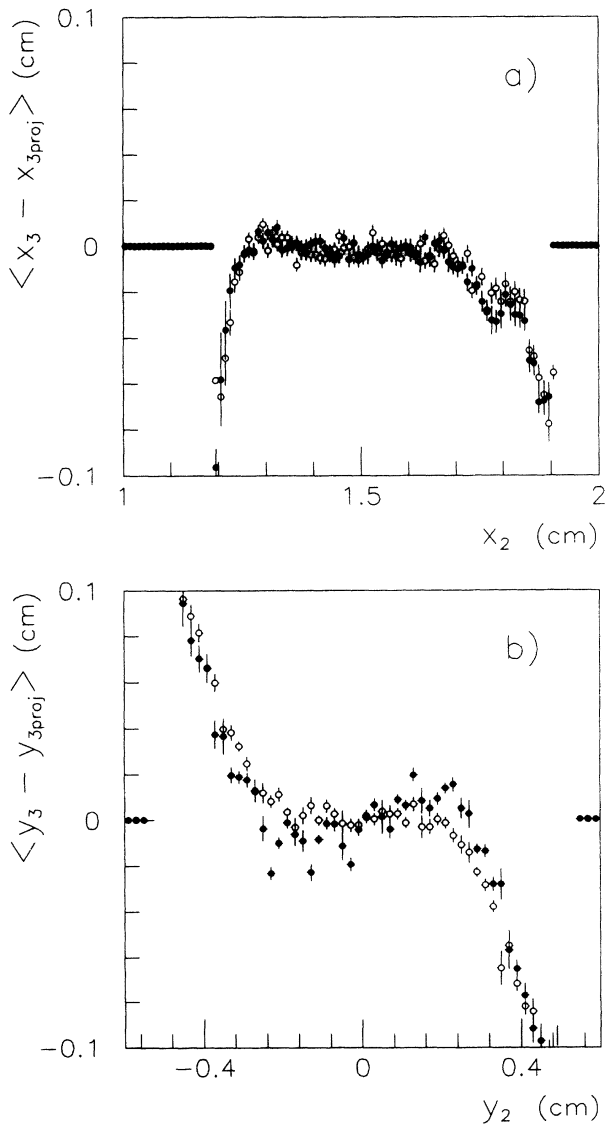


FIG. 21. Mean value of the difference between the coordinate measured by $S3$ and the projected value, calculated using the coordinate measured by $S2$ and assuming the interaction point to be at $(x, y, z) = (0, 0, 0)$, as a function of the coordinate measured by $S2$. (a) x coordinate and (b) y coordinate for (●) data at $\sqrt{s} = 546$ GeV and (○) simulation.

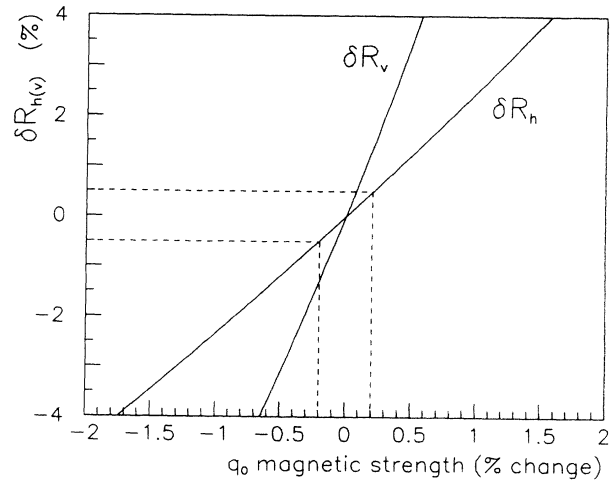


FIG. 22. Dependence of δR_h and δR_v on the percentage change of the strength of the q_0 magnets at $\sqrt{s} = 546$ GeV. $\delta R_{v(h)}$ is the percentage change of $R_{v(h)} = \frac{L_3^{v(h)}}{L_2^{v(h)}}$. The uncertainty on R_h (dashed lines) results in a 0.2% uncertainty on the low- β quadrupole magnetic strength.

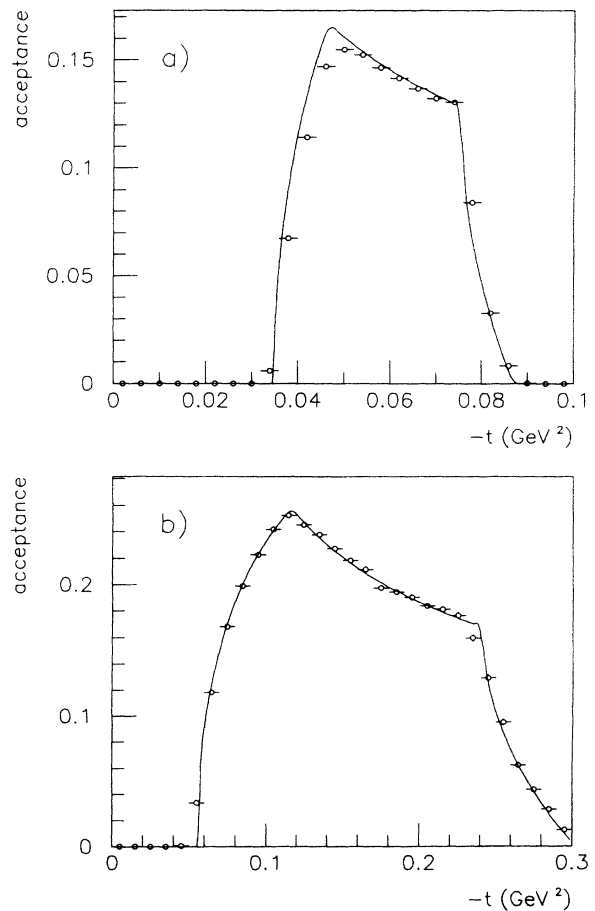


FIG. 23. Spectrometer t acceptance (○) calculated using the simulation, which accounts for all smearing effects at (a) $\sqrt{s} = 546$ and (b) $\sqrt{s} = 1800$ GeV. The solid line represents the t acceptance calculated with Eq. (D1) of Appendix D.

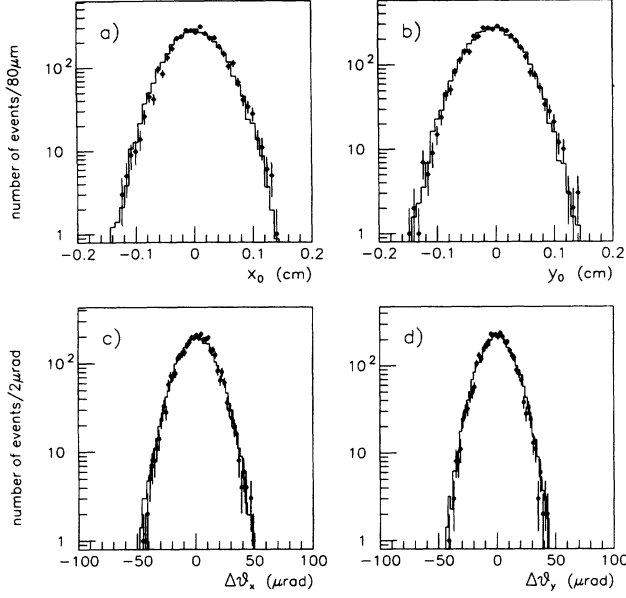


FIG. 24. Comparison of distributions from data (\bullet) and simulation ($-$) at $\sqrt{s}=1800$ GeV. (a), (b) Event origin (x_0, y_0); (c), (d) collinearity ($\Delta\theta_x, \Delta\theta_y$), where $\Delta\theta = \theta^P - \theta^{\bar{P}}$.

mm. With our alignment procedure, we corrected the detector positions for 0.1 mm offsets, working in the beam reference system. However, we noticed that, although in all three runs (one at $\sqrt{s}=546$ and two at $\sqrt{s}=1800$) the detectors were placed at about the same distance from the beam, the actual positions relative to the nominal beam axis differed by several millimeters among runs, indicating that the beam position (X_0, Y_0) at $z = 0$ and the beam angle (Θ_{0x}, Θ_{0y}) in the magnetic lattice frame were different in every run. The beam position with respect to the magnetic axis was determined for every run using the data. In the beam-axis reference system, for a given run r , we define $x_{0i}^r, y_{0i}^r, x_{1i}^r$, and y_{1i}^r as the coordinates of the center of detector i in arm 0 and arm 1, respectively. In the survey reference system, the center of detector i in the spectrometer arm j has coordinates x_{ji}^r and y_{ji}^r , and, for all runs, the same offsets δx_{ji} and δy_{ji} with respect to the magnetic lattice axis. Therefore, in the magnetic lattice reference system, the detector coordinates are

$$\begin{aligned} x_{ji}^{r'} &= x_{ji}^r + \delta x_{ji} = x_{ji}^r + X_0^r \epsilon_i^{hr} + L_i^{hr} \Theta_{0x}^r, \\ y_{ji}^{r'} &= y_{ji}^r + \delta y_{ji} = y_{ji}^r + Y_0^r \epsilon_i^{vr} + L_i^{vr} \Theta_{0y}^r, \end{aligned}$$

where (ϵ_i^r, L_i^r) are the transport matrix coefficients listed in Table I. For two different runs r and s , the quantities

$$\begin{aligned} \Delta_{ji}^{rs} &= x_{ji}^{r'} - x_{ji}^{s'} - x_{ji}^r + x_{ji}^s, \\ \Omega_{ji}^{rs} &= y_{ji}^{r'} - y_{ji}^{s'} - y_{ji}^r + y_{ji}^s, \end{aligned}$$

TABLE VIII. Beam parameters at the interaction point.

\sqrt{s}	σ_{x_0}	σ_{y_0}	$\sigma_{\Theta_x}^P$	$\sigma_{\Theta_x}^{\bar{P}}$	$\sigma_{\Theta_y}^P$	$\sigma_{\Theta_y}^{\bar{P}}$
	(μm)		(μrad)			
546	260.0	190.0	36.4	36.4	31.5	31.5
1800 (1st run)	290.0	200.0	6.0	4.0	6.0	4.0
1800 (2nd run)	250.0	250.0	2.9	3.2	2.9	3.2

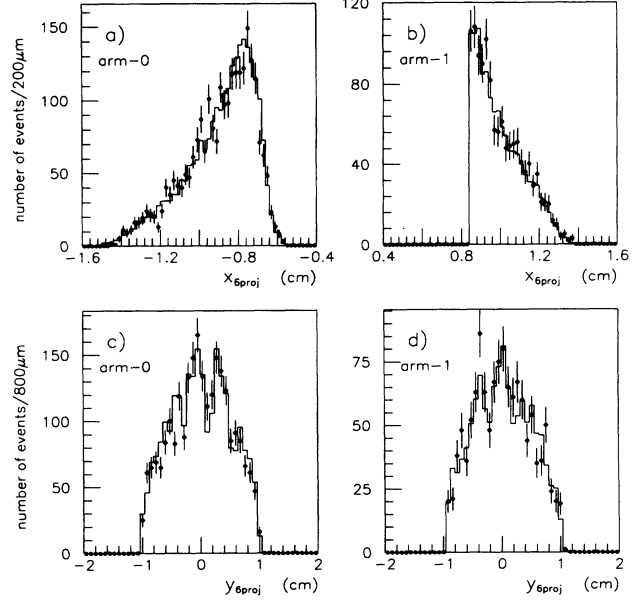


FIG. 25. Comparison of distributions from data (\bullet) and simulation ($-$) at $\sqrt{s}=1800$. (a), (b): $x_{6 \text{ proj}} = L_6^h \cdot \theta_x^P$; (c), (d): $y_{6 \text{ proj}} = L_6^h \cdot \theta_y^P$.

were known from survey and alignment with the data to better than 100 μm . We fitted all Δ_{ji}^{rs} and Ω_{ji}^{rs} values derived from all combinations of runs with the forms

$$\begin{aligned} \epsilon_i^{hr} X_0^r - \epsilon_i^{hs} X_0^s + L_i^{hr} \Theta_{0x}^r - L_i^{hs} \Theta_{0x}^s, \\ \epsilon_i^{vr} Y_0^r - \epsilon_i^{vs} Y_0^s + L_i^{vr} \Theta_{0y}^r - L_i^{vs} \Theta_{0y}^s, \end{aligned}$$

where the beam angle Θ_0^r and position (X_0^r, Y_0^r) in each run r were fit parameters. We derived $Y_0 = 0.0$ within 0.2 mm and $\Theta_{0y} = 0$ within 3 μrad in all runs. In the x - z magnetic lattice plane, we obtained

Run	X_0 (cm)	Θ_{0x} (μrad)
$\sqrt{s}=546$	0.1 ± 0.05	27.0 ± 2.6
first at $\sqrt{s}=1800$	0.02 ± 0.01	-8.0 ± 2.0
second at $\sqrt{s}=1800$	-0.25 ± 0.01	7.0 ± 2.0

This determination of the beam angle and position for each run was important for obtaining a momentum resolution $\simeq 0.1\%$ for the diffractive antiproton recoils with momentum smaller than that of the beam.

APPENDIX D: MONTE CARLO SIMULATION

Neglecting detector resolution and beam dispersion at the interaction point, the spectrometer acceptance α is a function of the four-momentum transfer $t = -p^2 \theta^2$:

$$\alpha = \begin{cases} 0 & \text{if } 0.0 < -t < (p\theta_x^{\min})^2, \\ \frac{1}{\pi} \arccos\left(\frac{\theta_x^{\min} p}{\sqrt{-t}}\right) & \text{if } (p\theta_x^{\min})^2 < -t < (p\theta_c)^2, \\ \frac{1}{\pi} \arcsin\left(\frac{\theta_y^{\max} p}{\sqrt{-t}}\right) & \text{if } (p\theta_c)^2 < -t < (p\theta'_c)^2, \\ \frac{1}{\pi} \left[\arcsin\left(\frac{\theta_y^{\max} p}{\sqrt{-t}}\right) - \arccos\left(\frac{\theta_x^{\max} p}{\sqrt{-t}}\right) \right] & \text{if } (p\theta'_c)^2 < -t < (p\theta_x^{\max})^2, \\ 0 & \text{if } (p\theta_x^{\max})^2 < -t, \end{cases} \quad (\text{D1})$$

where p is the beam momentum, θ is the elastic scattering angle, $\theta_c = \sqrt{(\theta_x^{\min})^2 + (\theta_y^{\max})^2}$ and $\theta'_c = \sqrt{(\theta_x^{\max})^2 + (\theta_y^{\max})^2}$. The angles $\theta_x^{\max(\min)}$ and θ_y^{\max} are the smallest (largest) of the maximum (minimum) angles $x_i^{\max(\min)}/L_i^h$ and y_i^{\max}/L_i^v covered by the detector i . The Monte Carlo simulation incorporates the smearing effect of the detector resolution and of the beam *trace space* at the interaction point. In the simulation, the beam profile and angular divergence at the interaction region were assumed to be Gaussian distributions; the widths $\sigma_{x,y}$ and $\sigma_{\theta_{x,y}}$ determined by flying wire mea-

surements of the beam emittance during the runs were adjusted by $\simeq 10\%$ in order to reproduce the measured collinearity and vertex distributions (see Table VIII). As shown in Fig. 23, the geometrical acceptances compare well to the ones derived by the complete simulation at $\sqrt{s}=546$ and 1800 GeV, indicating that smearing effects are small. Figure 24 compares the interaction point and collinearity distributions for data and simulation at $\sqrt{s}=1800$ GeV. At the same energy, Fig. 25 compares x and y distributions measured by all detectors and projected at the z position of $S6$ in each spectrometer arm for the data and for an equal number of simulated events.

- [1] CDF Collaboration, F. Abe *et al.*, following paper, Phys. Rev. D **50**, 5535 (1994).
- [2] CDF Collaboration, F. Abe *et al.*, this issue, Phys. Rev. D **50**, 5550 (1994).
- [3] S. Bertolucci *et al.*, Nucl. Instrum. Methods **A289**, 375 (1990).
- [4] G. Apollinari *et al.*, IEEE Trans. Nucl. Sci. **36**, 46 (1989).
- [5] R. Johnson, in Proceedings of the CERN-USA Accelerator School, Capri, Italy, 1988 (unpublished).
- [6] R. Castaldi and G. Sanguinetti, Annu. Rev. Nucl. Part. Sci. **35**, 351 (1985).
- [7] R. Cahn, Z. Phys. C **15**, 253 (1982).
- [8] UA4 Collaboration, M. Bozzo *et al.*, Phys. Lett. **147B**, 385 (1984).
- [9] UA4/2 Collaboration, M. Bozzo *et al.*, in *Results and Perspectives in Particle Physics*, Proceedings of Les Rencontres de Physique de la Vallée D'Aoste, La Thuile, Italy, 1993, edited by M. Greco (Editions Frontieres, Gif-sur-Yvette, 1993).
- [10] N. M. Amos *et al.*, Phys. Rev. Lett. **68**, 2433 (1992).
- [11] D. S. Ayres *et al.*, Phys. Rev. D **15**, 3107 (1977).
- [12] M. Ambrosio *et al.*, Phys. Lett. **115B**, 495 (1982); N. Amos *et al.*, *ibid.* **120B**, 460 (1983); N. Amos *et al.*, *ibid.* **128B**, 343 (1983).

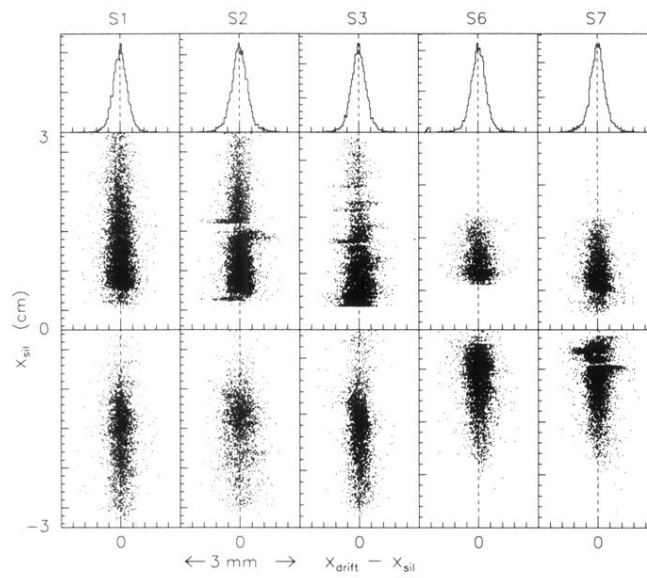


FIG. 14. Distribution of the difference between the x coordinate measured by the drift chamber (x_{drift}) and by the silicon (x_{sil}) vs x_{sil} for each spectrometer detector at $\sqrt{s}=1800$ GeV.

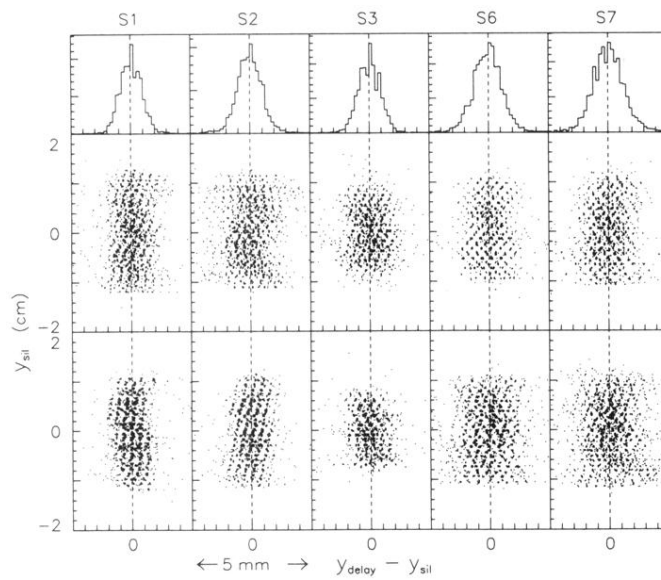


FIG. 15. Distribution of the difference between the y coordinate measured by the delay line (y_{delay}) and by the silicon (y_{sil}) vs y_{sil} for each spectrometer detector at $\sqrt{s}=1800$ GeV.

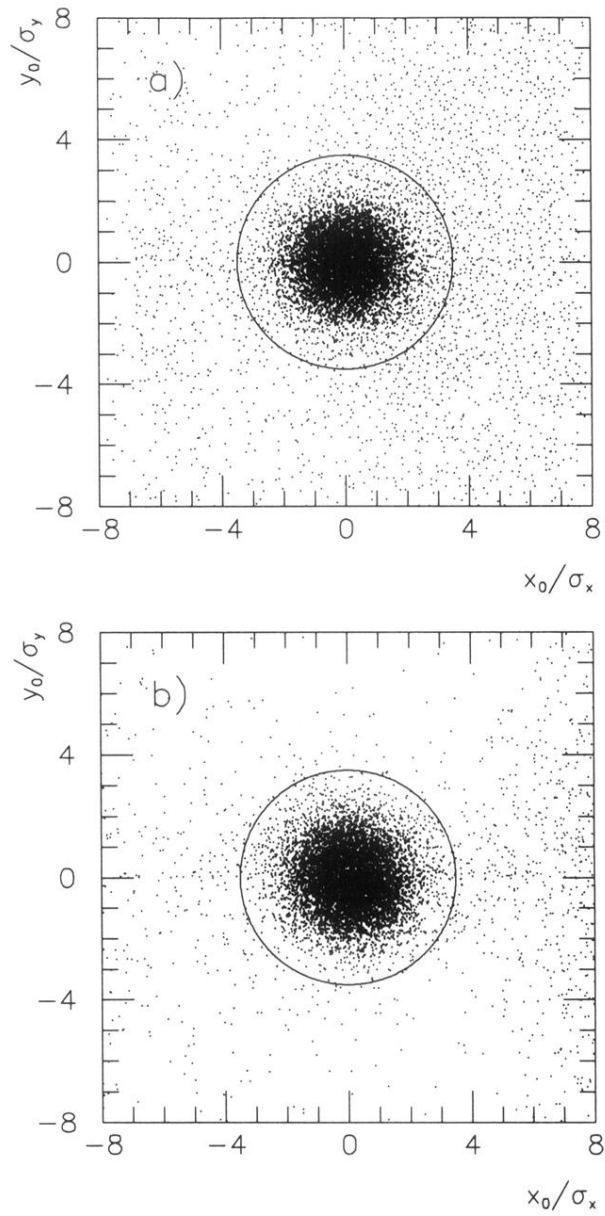


FIG. 3. Interaction point distributions in the transverse plane at $z = 0$ for (a) $\sqrt{s}=546$ and (b) $\sqrt{s}=1800$ GeV, in units of the reconstruction errors $\sigma_{x(y)}$ ($\simeq 350 \mu\text{m}$). The circle indicates the vertex cut.

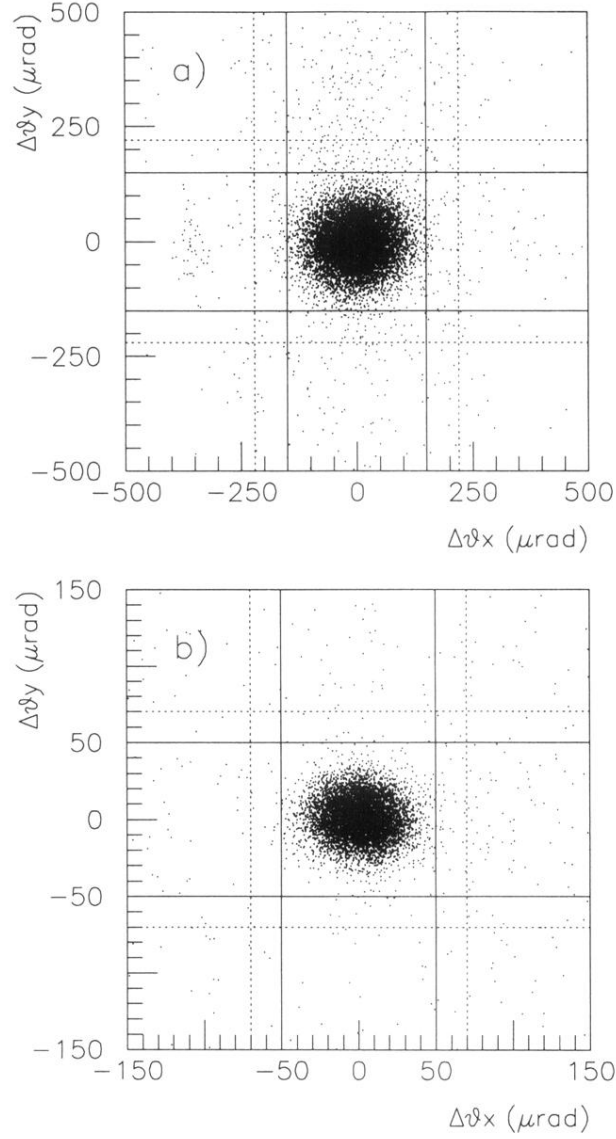


FIG. 5. Collinearity distributions ($\Delta\theta_y = \theta_y^{\bar{p}} - \theta_y^p$ vs $\Delta\theta_x = \theta_x^{\bar{p}} - \theta_x^p$) for events accepted by the vertex cut at (a) $\sqrt{s}=546$ and at (b) $\sqrt{s}=1800$ GeV. The solid lines indicate our collinearity cuts; events with $\Delta\theta_x$ outside the dashed lines are used to estimate the background contamination inside the collinearity cuts.